

Density and lithospheric thickness of the Tharsis Province from MEX MaRS and MRO gravity data

M. Beuthe,¹ S. Le Maistre,¹ P. Rosenblatt,¹ M. Pätzold,² and V. Dehant¹

Received 27 September 2011; revised 26 January 2012; accepted 21 February 2012; published 4 April 2012.

[1] Radio science tracking of Mars Express (MaRS experiment) and Mars Reconnaissance Orbiter produced high resolution Martian gravity data. Applying localized spectral analysis on the new gravity data sets, we study the surface density and lithospheric elastic thickness in the Tharsis province. The gravity signal is predicted with geophysical models either including bottom loading (top/bottom model) or taking into account the loading history (top/top model). Volcanic shields are mainly composed of high-density lava but their construction could have begun with lower density lava, with the exception of Ascræus Mons which has a top of lower density. Buoyant bottom loading may have been present in the form of a mantle plume under Olympus Mons. The elastic thickness was much larger at Olympus Mons than at other volcanoes, suggesting large spatial variations of heat flux during the Hesperian. Alternatively, small elastic thicknesses could be artifacts reflecting the presence of very localized high-density crustal intrusions beneath the volcanoes. Thaumasia highlands were probably supported by a mantle plume at the time of formation. In Valles Marineris, top/bottom models predict low densities and large elastic thicknesses, in conflict with the basaltic rock composition and Hesperian age of the valley. Dense mafic dikes underlie the western part of the valley. The top/top model serves to test another scenario in which the trough is formed with sedimentary infilling removed much later by erosion, the elastic thickness increasing in between. At the large volcanoes, the relation between gravity and topography is anisotropic probably because of density variations.

Citation: Beuthe, M., S. Le Maistre, P. Rosenblatt, M. Pätzold, and V. Dehant (2012), Density and lithospheric thickness of the Tharsis Province from MEX MaRS and MRO gravity data, *J. Geophys. Res.*, 117, E04002, doi:10.1029/2011JE003976.

1. Introduction

[2] On the Martian surface, geological events spanning more than 4 Ga are incredibly well preserved because of the lack of crust recycling (no plate tectonics) and the very slow erosion (no liquid water for ages). The landscape of Mars is thus dominated by two structures dating back to the epoch of large-scale impacts, namely the north-south dichotomy and the Tharsis bulge. These features are unique to Mars and their origin is a matter of debate. The Tharsis bulge is a huge topographic rise in the western hemisphere covering one fifth of the total planetary surface and reaching an altitude of 7 km (discounting volcanoes on top). It is characterized by large volcanic plains and shields with ages spanning the whole Martian history, radiating grabens thousands of kilometers long, and concentric wrinkle ridges. In its eastern part, the Tharsis bulge is radially cut by Valles Marineris, the largest canyon of the solar system.

[3] Most of the reconstruction of the history of Tharsis is based on information about the surface: stratigraphy, dating by crater counting, paleotectonic analysis, mineralogy and elemental composition from remote sensing. Three types of instruments probe the subsurface. Radars like MARSIS on Mars Express (MEX) and SHARAD on Mars Reconnaissance Orbiter (MRO) can in principle detect interfaces at a depth of several kilometers, but their signal does not penetrate easily into volcanic flows [Carter *et al.*, 2009], limiting their use in the Tharsis area. Crustal magnetization was measured by instruments on Mars Global Surveyor (MGS), with the conclusion that Tharsis is nearly completely demagnetized with respect to its surroundings [Johnson and Phillips, 2005; Jellinek *et al.*, 2008; Lillis *et al.*, 2009]. Finally, velocity perturbations of orbiting spacecraft constrain the subsurface density. Knowledge of the density is important to determine Tharsis composition (are there sediments besides lava flows?) and at greater depth for the understanding of crustal evolution [Nimmo and Tanaka, 2005]. Since the density structure is often modeled as various loads acting on an elastic lithosphere, density modeling with gravity data also yields estimates of the lithospheric thickness, which can be turned into estimates of the heat flux at the time of loading [McGovern *et al.*, 2002, 2004b; Ruiz *et al.*, 2011]. The heat flux is a crucial parameter constraining

¹Royal Observatory of Belgium, Brussels, Belgium.

²Rheinisches Institut für Umweltforschung, Abteilung Planetenforschung, Universität zu Köln, Cologne, Germany.

the thermal evolution of the planet and more specifically the state of the mantle under Tharsis. Knowing the heat flux is essential to evaluate possible scenarios of the bulge construction [Solomon and Head, 1990; Kiefer and Li, 2009; Grott and Breuer, 2010].

[4] Using the most recent Martian gravity data provided by low altitude orbiting spacecraft (pericenter between 255 km and 330 km), we determine with admittance methods the surface density and the lithospheric structure at various locations in the Tharsis province. The data sets are line-of-sight Doppler data [Beuthe et al., 2006; Pätzold et al., 2009] from the Mars Express Radio Science Experiment (MaRS) and the most recent global gravity field (MRO110B) of harmonic degree and order 110 based on measurements by MGS, Mars Odyssey and MRO [Konopliv et al., 2011]. These two data sets differ in essential ways and are thus complementary. MEX MaRS data are defined along one-dimensional tracks and are intrinsically local (due to the high eccentricity of the orbit). By contrast, the global gravity field is known everywhere outside the planet (making it two-dimensional for the purpose of gravity analysis), and must be localized by a window before analyzing a particular feature on the surface. Previous admittance studies of Tharsis with small windows used global gravity fields of maximum degree and order 80 [McGovern et al., 2002, 2004b] or 85 [Belleguic et al., 2005]. Extending the gravity field by 25 degrees makes a big difference for localized analysis because of the much larger range available for admittance fits.

[5] We choose to study surface features for which the gravity field is highly correlated with the topography, so that the gravity field can be predicted from the topography with mechanical models of lithospheric flexure. The selected areas are Olympus Mons, Tharsis Montes (Ascraeus, Pavonis, Arsia), Thaumasia highlands (Claritas and Coracis Fossae) and Valles Marineris. For completeness, we also analyzed the two remaining large volcanoes, namely Alba Mons (where the correlation is low at intermediate wavelengths) and Elysium Mons (outside the Tharsis province). We predict the gravity signal with two kinds of lithospheric flexure models: the bottom loading model in wide use and the new top/top model which considers the loading history.

2. Data

2.1. MEX MaRS

[6] Mars Express is in orbit around Mars since 25 December 2003. Its orbit is quasi-polar (inclination between 86.6° and 86.8°) and very eccentric (initial eccentricity of 0.607, changed to 0.57 in May 2004). The orbital period was between 6.7 and 6.9 h from 2004 to 2009, when target gravity experiments ended. The experiment MaRS performs different types of measurements: atmospheric and ionospheric sounding with radio occultations, solar corona sounding, bistatic radar, target gravity and Phobos gravity flybys [Pätzold et al., 2004, 2009]. The principle of target gravity was suggested by the very elliptical orbit of the spacecraft which results in altitudes varying by a factor 40. The effect of gravity anomalies on the spacecraft decreases as a power law depending on the anomaly wave number ℓ and on the ratio of the altitude h to the planetary radius R : $g_\ell \sim (1 + h/R)^{-\ell-2}$.

Gravity anomalies of long wavelength ($\lambda \sim 2\pi R/\ell$) thus affect the whole spacecraft trajectory but anomalies of short wavelength only perturb the spacecraft's velocity near pericenter. Target gravity experiments study short wavelength velocity perturbations near pericenter when the pericenter is located above a target of geophysical interest. In the equatorial region, the altitude of the pericenter changed from about 275 km in 2004 to 330 km in 2009, leading to a 50% decrease of the corresponding gravity perturbation at harmonic degree $\ell = 51$. Since anomalies of short wavelength are mainly due to surface density variations, the experiment constrains the surface density in the target area. Figure 1 shows the location of pericenters in the Tharsis province while Table 1 gives the orbit numbers of the gravity passes at Olympus Mons, Ascraeus Mons and Valles Marineris used in our analysis.

[7] Characteristics and examples of gravity data are described in Beuthe et al. [2006] and Pätzold et al. [2009]. Observed Doppler shifts are proportional to the velocity variation along the line-of-sight direction and are measured with a sampling time of 1 s in coherent X-band. They are reduced to Doppler residuals (and then transformed into velocity residuals) by subtracting the predicted Doppler shift based on the reconstructed orbit of MEX provided by the European Space Operation Center (ESOC). Since ESOC computes the orbit of MEX with the global gravity field JGM85F02 up to degree and order 50, velocity residuals do not include contributions of lower degree gravity harmonics. Figure 2 shows velocity residuals and filtered acceleration residuals for the orbit 7173 above Ascraeus Mons. Pätzold et al. [2009] discuss predictions of the total noise and solar plasma contribution for three global gravity experiments at the orbit's apocenter. Beuthe et al. [2006] already compared the noise on velocity residuals of MEX MaRS and MGS. Updating this analysis to all target gravity passes (2004–2009), we compute an average noise of 0.051 mm/s (at a sampling time of 10 s), which compares well with the average data noise of 0.053, 0.056 and 0.040 mm/s for MRO, MGS and Mars Odyssey, respectively [Konopliv et al., 2011].

2.2. Global Gravity Field

[8] The orbit of MRO is nearly circular (255–320 km) so that orbital perturbations due to gravity anomalies are not naturally windowed by pericenter passes above targets. We will thus not analyze MRO orbits in the same way as MEX orbits, using instead the 2D gravity field generated from them. Data inversion yields a global solution for the gravity field of the planet expressed as a spherical harmonic expansion up to maximum degree ℓ_{\max} . The solution is however not physically meaningful up to ℓ_{\max} . Its global resolution is given by the degree ℓ_{resol} at which the formal error of the inversion becomes larger than the associated gravity coefficient. As gravity is expected to be highly correlated with topography at small scale, the resolution can also be estimated by the degree at which this correlation is smaller than a specified threshold [e.g., Wieczorek, 2007]. The two methods give similar resolutions if the correlation threshold is chosen to be about 0.6–0.7.

[9] Previous localized admittance studies were based on gravity fields from MGS and Mars Odyssey, with a

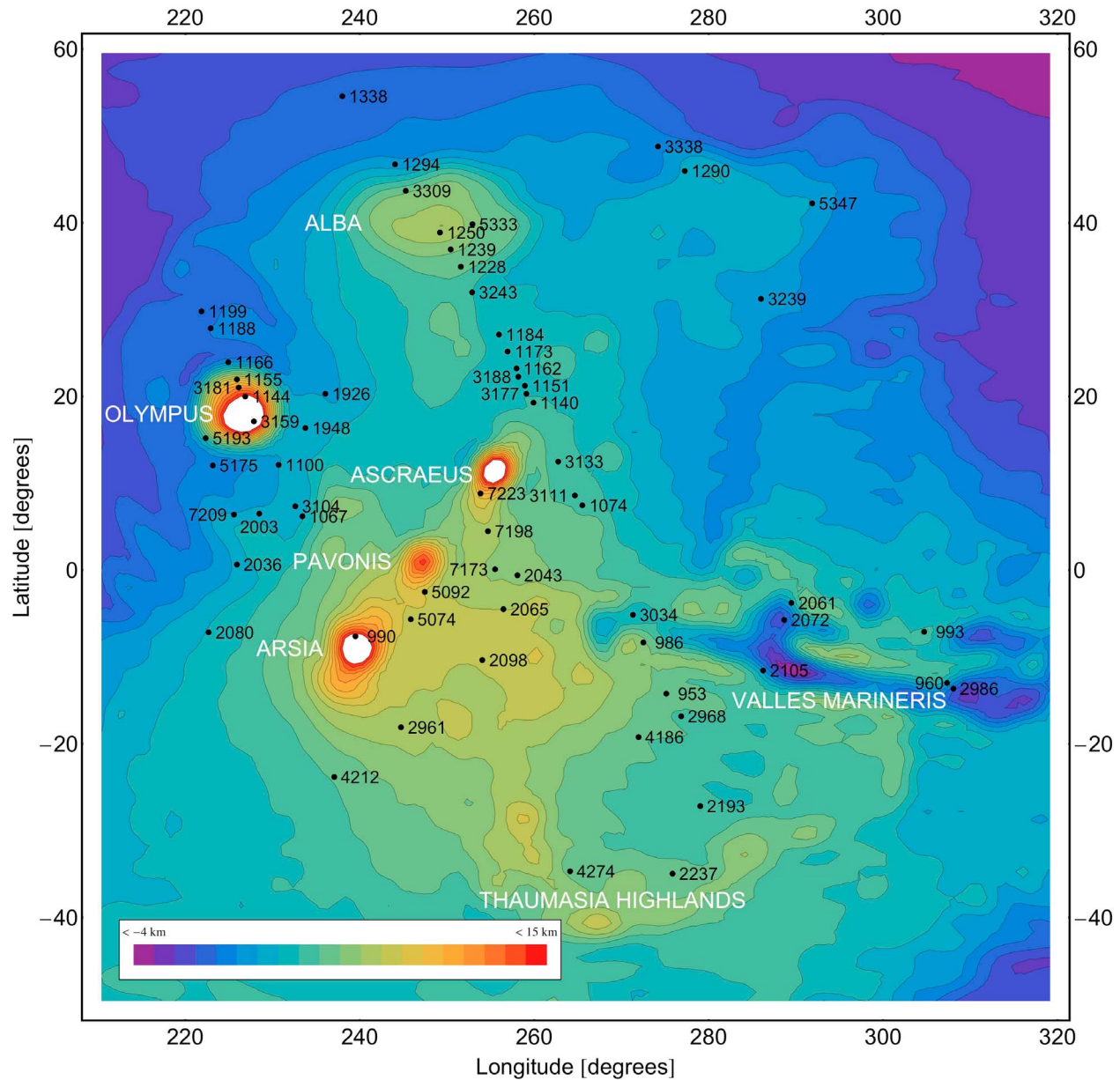


Figure 1. Pericenters of gravity passes observed with MEX MaRS in the Tharsis province, superimposed on the topography defined in section 2.3. Contours are spaced by 1 km between -4 km and $+15$ km (elevations above 15 km are saturated in white).

resolution $\ell_{\text{resol}} \approx 60$ [McGovern *et al.*, 2002, 2004b] or $\ell_{\text{resol}} \approx 65$ [Belleguic *et al.*, 2005]. MRO has a lower mapping altitude (255–320 km) than MGS and Mars Odyssey (370–450 km) so that Konopliv *et al.* [2011] could improve the

resolution up to $\ell_{\text{resol}} \approx 90$ in the latest gravity solutions MRO110B and MRO110B2. The latter solution differs from the former by the looser a priori constraint applied on the amplitude of high harmonic degrees. Since the

Table 1. Orbit Numbers of Pericenter Passes Above Selected Targets^a

Target	Orbit Numbers	Total
Olympus Mons	1067, 1100, 1144, 1155, 1166, 1188, 1199, 1926, 1948, 2003, 2036, 3104, 3159, 3181, 5175, 5193, 7209	17
Ascræus Mons	1074, 1140, 1151, 1162, 1173, 1184, 2043, 2065, 3111, 3133, 3177, 3188, 7173, 7198, 7223	15
Valles Marineris	960, 986, 993, 2061, 2072, 2105, 2986, 3034	8

^aAttribution to a certain target is often ambiguous if only pericenter coordinates are used but in most cases the effect of the target is obvious in the acceleration residual (see, e.g., Figure 2).

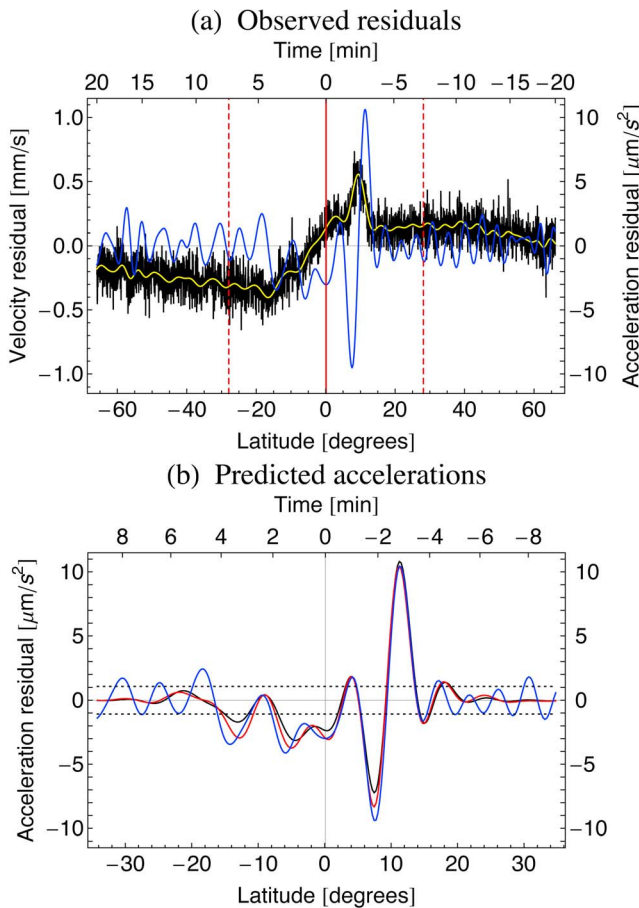


Figure 2. Pericenter pass (orbit 7173) above Ascræus Mons. (a) Observed velocity residual at 1-s sampling (black) and filtered at 70 s (yellow), observed acceleration residual filtered at 70 s (blue). The central red line indicates the position of the pericenter (lat. = 0.1°N) while the dashed red lines mark the boundaries of the zone with altitudes lower than 500 km. (b) Acceleration residual as observed by MEX MaRS (blue), as predicted by the global gravity field (red), as predicted by the uncompensated topography with a density of 2.9 g/cm³ (black) and finite amplitude corrections. The dotted lines show the filtered acceleration noise (±1.08 μm/s²) which is determined from the high altitude part of the profile.

resolution of the gravity field is not uniform, *Konopliv et al.* [2011] also give a map of the local resolution, or *degree strength* (see their Figure 10), defined as the crossing point between the expected gravity signal (from Kaula rule) and the localized gravity error. The minimum degree strength is 86 in the northern midlatitude region where the volcanoes Olympus, Alba and Elysium Montes are located. However this procedure underestimates the resolution at the volcanoes because the gravity signal is much larger at these locations than Kaula rule's prediction. We thus assume that the resolution reaches everywhere $\ell_{resol} = 90$.

[10] In 2D analysis, the global gravity field is MRO110B whereas the field serving for comparison in the 1D analysis of MEX MaRS residuals is the first version (MRO95A) of

the solution including MRO data [*Konopliv et al.*, 2011]. These two fields have a correlation above 0.9 up to degree 80 so that their difference is negligible when computing the expected acceleration along MEX orbit. Following common practice [*Neumann et al.*, 2004], the gravity signal in 2D analysis is evaluated at radius $R = 3396$ km which is the reference radius for the expansion of the gravity field in spherical harmonics (predictions from models are also computed at this radius). Spherical harmonic coefficients of the global gravity fields are archived with the Planetary Data System (PDS) Geoscience Node [*Wieczorek*, 2007]. We perform spherical harmonic expansions, reconstructions, rotations and spherical multitaper spectral analysis with the software SHTOOLS [*Wieczorek*, 2007].

2.3. Topography

[11] The lithosphere is loaded by the topography which is defined as the difference between the planetary shape and geoid. The Mars Orbiter Laser Altimeter (MOLA) aboard MGS measured the Martian shape at much higher resolution than the gravity field [*Smith et al.*, 2001]. Its spherical harmonic coefficients are available up to degree and order 719 as *MarsTopo719.shape* [*Wieczorek*, 2007]. The Martian geoid (or areoid) is computed from the gravity field with a reference radius equal to the mean radius of the planet (3389.5 km). The mean equatorial radius of the resulting areoid is equal to 3395.45 km, that is 550 m smaller than the areoid used to define elevations on MOLA maps [*Neumann et al.*, 2004]. Our topographic elevations are thus 550 m higher than those of MOLA.

[12] *Plescia* [2004] defines the reference surface of volcanoes by the lowest elevation at which there is a change in slope; it can be obtained from the difference (Summit Elevation - Relief) in his Table 1. Bearing in mind that our elevations are 550 m higher than MOLA elevations (see section 2.3 for details), we obtain -0.25/3.75/6.15/6.55/1.55/2.05 (in km) for the reference surfaces of Olympus/Ascræus/Pavonis/Arsia/Alba/Elysium. Since the topography is gridded, summit elevations depend on the grid resolution. With a maximum harmonic degree equal to 110, maximum heights are 21.7/19.5/13.7/18.2/6.8/8.8 (in km) for the respective volcanoes.

[13] The topography of Valles Marineris is defined as follows. We fill the valley system up to the rims in order to get the topography of Mars without Valles Marineris. The filling is done by joining opposite rims with straight lines in a coordinate grid oriented so that one axis is along the main strike of the faulting system. Since the valley system can be divided into two subsets with different orientations, we successively apply two rotations on the coordinate grid. Let A , B and C be the points with coordinates (7°S, 275°E), (15°S, 307°E) and (6°S, 330°E), respectively. The first subset of Valles Marineris, from 260–270° to 307° of longitude, is oriented along the great circle going through A and B , whereas the second one, from 307° to 330–335° of longitude, is oriented along the great circle going through B and C . The difference between the 'filled' topography and the original one is the topography of Valles Marineris shown on Figure 3. The volume of 6.25×10^6 km³ is compatible with the estimate of *Davis and Andrews-Hanna* [2011] but larger than the one in *Lucchitta et al.* [1994] because

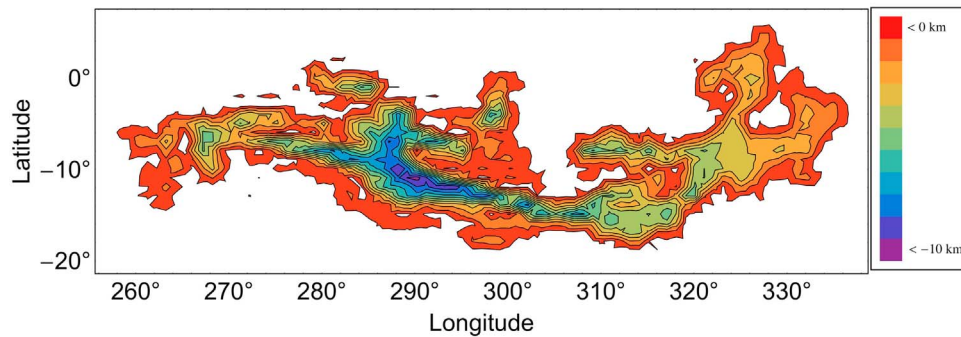


Figure 3. Topography of Valles Marineris obtained by filling its canyons to the rim. Contours are spaced by 1 km, and vary between 0 km and -10 km. Topography between 0 and -0.2 km has been set to zero in order to eliminate ringing artifacts, so that the first contour is effectively shifted to -0.2 km. Topography above 0 km is negligible.

the latter considered a canyon less extended in longitude and used pre-MOLA topography.

3. Tools

3.1. Localized Spectral Analysis

3.1.1. Motivation

[14] An infinite number of different density configurations within the planet can result in the same observed gravity field. In crustal thickness modeling, a unique solution is reached by assuming that the only non-uniform parameter is the crustal thickness [Neumann *et al.*, 2004]. However density variations certainly exist at small scale and maybe also at the largest Martian scale, that is the hemispheric dichotomy [Belleguic *et al.*, 2005; Pauer and Breuer, 2008]. Another class of models (used in this paper) is based on the concept of lithospheric flexure - including isostatic compensation as a subclass - in which the gravity signal can be predicted from the knowledge of the topography plus the values of a finite number of parameters such as the thickness of the lithosphere and crust, the density of the crust and load, etc. Model parameters are expected to be spatially dependent but it is not possible to leave them all free without falling back on the problem of non-uniqueness.

[15] As a way out, localization consists in restricting the modeling to a region of limited extent in which the model parameters are assumed to be constant. Since the orbit of MEX is very eccentric, gravity anomalies mainly affect MEX MaRS acceleration residuals in the pericenter area, which means that these data are naturally windowed. By contrast the global gravity field must be localized by multiplication with a smooth window (tapering) before analyzing a particular feature on the surface. In the tapering approach, the window should not only be near zero outside the targeted region but also band-limited in the spectral domain so as to minimize spectral leakage [Percival and Walden, 1993].

[16] Since the power of gravity anomalies decreases as wavelengths get shorter (see section 2.1 and Figure 4), the signal in the spatial domain is dominated by long wavelengths (after having filtered very short wavelengths due to noise in MEX MaRS residuals). We thus transform the signal into the spectral domain and compute the gain factor or the admittance (transfer function between gravity and topography),

which has also the advantage of eliminating the gravity noise uncorrelated with topography [e.g., Wieczorek, 2007]. Good spectral estimates are obtained with the multitaper method, which consists in constructing a series of tapers, or optimal orthogonal windows, over which the spectrum is averaged.

3.1.2. The 1D Case

[17] MEX MaRS gravity passes are not sufficiently dense to warrant a 2D spectral analysis in targeted areas. The profiles will thus be individually analyzed with 1D spectral analysis. The acceleration residuals are naturally windowed by the rapidly increasing altitude of the spacecraft away from the pericenter, with gravity anomaly effects ($\ell > 50$) becoming negligible at altitudes higher than 500–600 km (Figure 2). The amplitude of the $\ell = 51$ gravity harmonic is about 100 times (resp. 40 times) weaker at an altitude of 600 km than at the pericenter altitude of 270 km (resp. 330 km). In order to minimize the influence of the noise, we extract from the profile the pericenter pass, that is the low altitude part of the orbit where gravity anomalies have the largest impact.

[18] As a rule of thumb, gravity experiments are not sensitive to wavelengths shorter than the pericenter altitude, say 280 km. Such a distance is covered at pericenter in approximately 70 s. Since geophysical effects are not expected at frequencies higher than 1/70 Hz, the original 1-s sampling time is unnecessarily small. Before resampling the signal, we filter it in order to avoid aliasing with a low-pass Kaiser-Bessel nearly equal ripple filter [Kaiser and Reed, 1977]; the cutoff is 1/10 Hz (it should be larger than $1/2\Delta t$, where Δt is the new sampling time). Next, we compute acceleration residuals by applying centered finite differences to the filtered velocity residuals. We then resample acceleration residuals with a 4-s time step in order to reduce the number of points to be examined, and interpolate them with a uniform spacing of 16 km along the ground track. Finally, we extract the pericenter pass defined by 256 points centered around the pericenter, which approximately correspond to a maximum altitude of 500–600 km and cover exactly 4096 km on the ground.

[19] The next step consists in comparing the observed acceleration residuals a with those predicted by the contribution of the surface topography alone, denoted t . We thus project along the line-of-sight (LOS) direction the

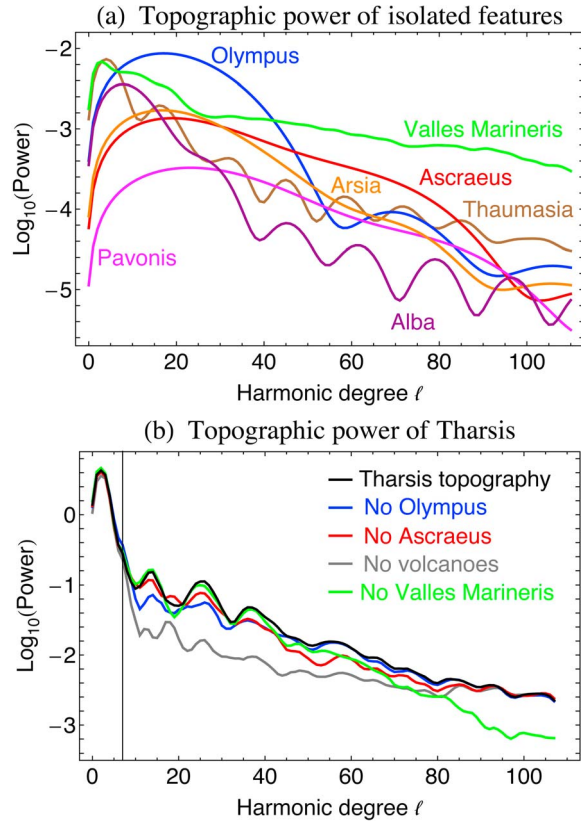


Figure 4. Influence of individual features on the topography: (a) topographic power spectrum of isolated volcanoes, Thaumasia highlands and Valles Marineris; (b) topographic power spectrum of the Tharsis province with specific features removed. Volcanoes are defined with respect to their reference surface (see section 2.3), Thaumasia highlands as the topography above 3 km within the circle of 20° angular radius centered in (33°S, 274°E) and Valles Marineris as in section 2.3. The topography of Tharsis is isolated by multiplying the global topography with an optimal spherical window (normalized to 4π on the sphere) defined by $(\theta_0, \ell_{win}) = (60^\circ, 3)$ and centered at (5°N, 260°E). ‘No volcanoes’ means the topography of Tharsis without Olympus, Ascræus, Pavonis, Arsia and Alba Montes. The vertical line at $\ell = 7$ indicates the degree under which the power is mainly due to the global Tharsis rise.

acceleration vectors predicted by the uncompensated topography (with a density of 2.9 g/cm³) at each spacecraft position [McKenzie and Nimmo, 1997; McKenzie et al., 2002]. If n is the noise, we write

$$\tilde{a}(k) = e^{i\phi} Z(k) \tilde{t}(k) + \tilde{n}(k), \quad (1)$$

where the tilde denotes the Fourier transform (the phase ϕ ensures that $Z(k)$ is real). The linear relation between two signals can be studied through the coherence $\gamma^2(k)$ and gain factor $Z(k)$ [Bendat and Piersol, 2000]. If the noise n is uncorrelated with a , the coherence represents the portion of the power spectrum of a that is contributed by t at wave number k . Since the relationship between a and t is only

linear in the limit of short wavelengths, the function $Z(k)$ can vary between profiles.

[20] The coherence and gain factor between a and t are estimated with

$$\gamma^2(k) = \frac{|S_{at}(k)|^2}{S_{aa}(k)S_{tt}(k)}, \quad (2)$$

$$Z(k) = \frac{|S_{at}(k)|}{S_{tt}(k)}, \quad (3)$$

where $S_{ij}(k)$ is the cross power spectrum density of the variables i and j . Power spectral densities and cross-spectral densities are estimated with the multitaper method using seven tapers [Percival and Walden, 1993; Simons et al., 2000]. The coherence is the square of the correlation $\gamma(k)$ and varies between 0 and 1. The variance of the gain factor is estimated [Bendat and Piersol, 2000] as

$$\sigma_Z^2(k) = \frac{1 - \gamma^2(k)}{2N} \left(\frac{Z(k)}{\gamma(k)} \right)^2, \quad (4)$$

where $N = 7$ is the number of tapers.

[21] According to the rule of thumb mentioned above, the pericenter altitude (270–330 km) determines the shortest wavelength due to gravity anomalies in the signal. The fitting range will thus be limited to the 13 longest wavelengths, so that the shortest wavelength is $4096/12 = 341$ km.

[22] It should be realized that the wavelengths λ_1 appearing in the 1D spectral analysis of the LOS acceleration residuals cannot be identified with the 2D wavelengths λ_2 of the gravity anomalies at the surface of the planet. The reason is that a gravity anomaly whose wave vector is not aligned with the ground track gives rise to LOS acceleration perturbations with $\lambda_1 \geq \lambda_2$. As an extreme example, the gravity anomaly whose wave vector is orthogonal to the ground track does not perturb the velocity of the spacecraft. Conversely, the LOS acceleration residual at wavelength λ_1 receives contributions from gravity anomalies with $\lambda_2 \leq \lambda_1$. This effect leads to the presence of long wavelengths in the 1D spectral analysis even when residuals are computed with respect to $\ell = 50$ (long wavelengths also appear because of variations in the altitude but the effect is minor). Thus long wavelengths λ_1 represent transverse contributions whereas short wavelengths λ_1 result from both longitudinal and transverse gravity anomalies. In conclusion, the 1D spectral analysis is intrinsically anisotropic.

3.1.3. Spherical Case

[23] Localized spectral analysis on the sphere is described in Simons et al. [1997], McGovern et al. [2002] and Wiczeorek and Simons [2005]. First the 2D gravity and topography (or shape) fields are multiplied in the spatial domain by a window defined on the sphere and expanded in spherical harmonics with coefficients $\Gamma_{\ell m}$ and $\Psi_{\ell m}$, respectively. The cross-power spectrum of the localized fields depends on the harmonic degree ℓ :

$$S_{\Psi\Gamma}(\ell) = \sum_m \Psi_{\ell m} \Gamma_{\ell m}, \quad (5)$$

Table 2. Spatospectral Windows for the 2-D Localized Admittance Analysis^a

Target	Latitude (°)	Longitude (°)	θ_0 (°)	ℓ_{win}
<i>Large Volcanoes</i>				
Olympus	18.40	226.00	15	16
Ascraeus	11.76	255.50	10	25
Pavonis	0.79	246.60	10	25
Arsia	-8.30	238.90	10	25
Alba	39.79	250.18	15	16
Elysium	24.74	146.90	15	16
<i>Thaumasia Highlands</i>				
Claritas	-34.00	262.00	10	25
Coracis	-32.00	286.00	10	25
<i>Valles Marineris (VM)</i>				
Far West	-7.00	270.00	10	25
Middle West	-8.00	288.00	15	16
Middle East	-12.00	308.00	15	16
Far East	-2.00	325.00	15	16
Global	-10.00	300.00	35	6

^aWindows are characterized by their center (latitude and longitude), angular radius θ_0 and maximum harmonic degree ℓ_{win} . Coordinates of volcanic targets are in planetocentric latitude with east longitude (USGS Gazetteer of Planetary Nomenclature). Other windows are located so as to maximize the coverage of high correlation areas (see Figure 5).

where the summation on harmonic order m includes both cosine and sine coefficients. The correlation $\gamma(\ell)$, admittance $Z(\ell)$, and variance of the admittance $\sigma_Z^2(\ell)$ are estimated with

$$\gamma(\ell) = \frac{S_{\Psi\Gamma}(\ell)}{\sqrt{S_{\Psi\Psi}(\ell)S_{\Gamma\Gamma}(\ell)}}, \quad (6)$$

$$Z(\ell) = \frac{S_{\Psi\Gamma}(\ell)}{S_{\Psi\Psi}(\ell)}, \quad (7)$$

$$\sigma_Z^2(\ell) = \frac{1 - \gamma(\ell)^2}{2\ell} \left(\frac{Z(\ell)}{\gamma(\ell)} \right)^2. \quad (8)$$

The formula for $\sigma_Z(\ell)$ is equivalent to the least squares error on $Z(\ell)$ if 2ℓ is replaced by $2\ell + 1$. The correlation varies between -1 and $+1$ and should be close to 1 for lithospheric flexure models without random bottom loading (see section 3.2.2). Note the similarity between 1D formulas (2)–(4) and 2D formulas (6)–(8). Summing on the harmonic order m in equation (5) reduces the noise, but any admittance anisotropy also disappears in the process. If the admittance is computed with a subset of all available coefficients (anisotropic admittance), one must adapt the factor 2ℓ in equation (8) to the number of coefficients in the subset.

[24] *Wieczorek and Simons* [2005] developed the multi-taper method on the sphere by finding band-limited windows whose power is maximally concentrated within the region of interest. The three requirements of small window size, high concentration and limited bandwidth are often in conflict. On the one hand, the localization of Martian volcanoes requires small windows (angular radius of 10 – 15°). On the other hand, the window bandwidth ℓ_{win} should be much smaller than ℓ_{resol} because localized harmonic coefficients are only reliable between $\ell_{win} + 3$ and $\ell_{resol} - \ell_{win}$ [*Wieczorek and Simons*, 2005]. Hence there is only one taper that is

concentrated enough (99%) for our purpose, reducing multitapering to a particular case of windowing [*Belleguic et al.*, 2005; *Wieczorek*, 2008].

[25] Since small windows reduce the range of reliable harmonic degrees, one should choose the largest window including the target but excluding significant contributions from neighboring features. Figure 4a shows the topographic power spectrum $S_{\Gamma\Gamma}(\ell)$ of important features of the Tharsis province, while Figure 4b shows the power of Tharsis topography once specific features are removed. Olympus Mons dominates the power between $\ell \approx 5$ and $\ell \approx 40$, whereas Valles Marineris is dominant at higher degrees. Admittance analysis should thus be done separately for each feature, otherwise the signal of weaker features will be drowned by the stronger ones.

[26] We follow the choice of *Belleguic et al.* [2005] for the window characteristics (see Table 2). *Belleguic et al.* [2005] choose the lower threshold of reliability to be $\ell_{win} + 7$ because the first 6 degrees are mainly due to the Tharsis rise (see Figure 4b) which can have a different elastic thickness than the volcanoes. The threshold could be even higher if the influence of the Tharsis rise extends to degrees 9 – 10 [*Wieczorek and Zuber*, 2004]. We set $\ell_1 = \ell_{win} + 7$ for top/bottom models but keep $\ell_1 = \ell_{win} + 3$ for top/top models because two elastic thicknesses are available in the latter models (see section 3.2). The misfit is thus computed in the range $\ell_{win} + 3$ (or $\ell_{win} + 7$) and $\ell_{resol} - \ell_{win}$, with $\ell_{resol} = 90$ (see section 2.2). The high resolution of the global gravity field MRO110B allows us to use a much wider spectral range in the fit with respect to past studies. For the 10° (resp. 15°) window, the spectral range available for fitting is four (resp. two) times the one used in *Belleguic et al.* [2005].

[27] Lithospheric flexure models may only be applied if gravity and topography are highly correlated. Figure 5 shows the localized correlation between gravity and planetary shape using an isotropic window with $(\theta_0, \ell_{win}) = (10^\circ, 25)$ centered every two degrees. Since the localized correlation depends on the wavelength, it has been averaged over the range $\ell_{win} + 3$ and $\ell_{resol} - \ell_{win}$, i.e. $28 \leq \ell \leq 65$. Regions of high correlation (above 0.9) are the large volcanoes except Alba Mons, Thaumasia highlands (Claritas Fossae and Coracis Fossae areas), Valles Marineris and scattered patches in the southern highlands. We will study all sites with high correlation in the Tharsis province (Figure 5 and Table 2), to which we add for completeness Alba Mons (where the correlation is low) and Elysium Mons (outside Tharsis province).

3.2. Geophysical Models

3.2.1. General Characteristics

[28] We parameterize the relation between gravity and topography with geophysical models based on the spherical thin elastic shell formulation of lithospheric flexure [*Turcotte et al.*, 1981; *McGovern et al.*, 2002; *Belleguic et al.*, 2005]. In essence, the crust and upper mantle are stratified in layers of constant density which are deflected by the action of various external and internal loads. These loads are usually taken to be the topographic load (see section 2.3) and an internal load called ‘bottom loading’. The total gravity signal is the sum of the contributions due to all density interfaces [*McGovern et al.*, 2002] and is computed at the same radius

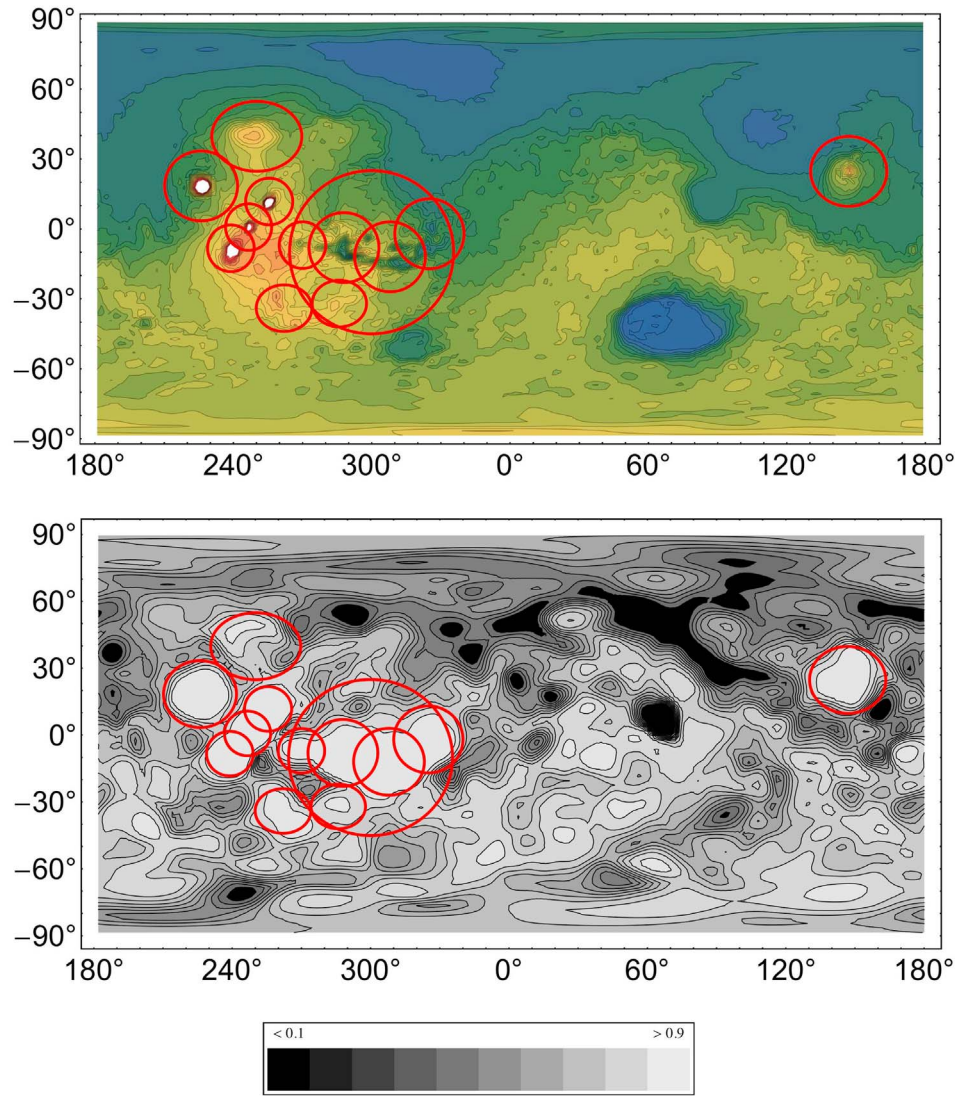


Figure 5. The top panel shows the localizing windows used in the spatio-spectral analysis (see Table 2) superimposed (in red) on a map of the Martian topography. The bottom panel shows the same localizing windows superimposed on a map of the localized correlation between gravity and planetary shape using an isotropic window with $(\theta_0, \ell_{win}) = (10^\circ, 25)$ centered every two degrees. The correlation is averaged over the range $\ell_{win} + 3$ and $\ell_{resol} - \ell_{win}$, i.e. $28 \leq \ell \leq 65$. Correlation contours are spaced by 0.1. Negative correlations are saturated in black.

$R = 3396$ km as the one chosen for the observed gravity signal. Finite amplitude corrections [Wieczorek and Phillips, 1998] must be included when computing the gravity anomaly because of the high elevation of Martian volcanoes. The internal load should in principle be defined with respect to the internal areoid, but its exact computation is laborious [Belleguic et al., 2005]. Actually, a good knowledge of the internal areoid is not crucial if the localizing window is small. Long wavelength features have indeed a minor influence in the limited spectral range used in local analysis (especially if the lower threshold is $\ell_{win} + 7$). We thus assume here that the internal areoid is identical to the surface areoid, apart from the degree 0 coefficient which is given by the mean radius of the interface. Note that the

areoid must be added to the relief of each deflected density interface before computing finite amplitude corrections. The harmonic degree 1 is fully compensated ($C_x(1) = 1$, see equation (A2)) by a variation in crustal thickness; it is taken into account at the surface and Moho when computing finite amplitude corrections.

[29] The construction of a model involves several choices: (1) How many density interfaces are there and at which depth? (2) Is the bottom load within the crust, at the Moho or deep within the mantle? What is its density anomaly? (3) Is it correct to treat the loading as an instantaneous event?

3.2.2. Top/Bottom Models

[30] We first consider models similar to the ones used by McGovern et al. [2002] and Belleguic et al. [2005] which

Table 3. Parameter Ranges for 2D Gravity Analysis^a

Parameter		Top/Bottom Models		Top/Top Models		Units
Name	Symbol	Value	Increment	Value	Increment	
Crust thickness	T_c	0–100	10	45	-	km
Crust density	ρ_c	2/2.5–3.4	0.1	2.9	-	g/cm ³
Density of load 1	ρ_{l1}	2/2.5–3.4	0.05	2/2.5–3.4	0.05	g/cm ³
Density of load 2	ρ_{l2}	-	-	2/2.5–3.4	0.05	g/cm ³
Elastic thickness for load 1	T_{e1}	0–200	10	0–200	20	km
Elastic thickness for load 2	T_{e2}	-	-	0–200	20	km
Base ^b	h_b	-	-	$h_b^{\min} - h_b^{\max}$	1	km
Bottom loading ratio ^c	f, f'	0–1	0.1	0	-	-

^aIn top/top models, load 1 and load 2 refer to the load under and above the base, respectively (load 2 is indistinguishable from load 1 in top/bottom models). The minimum density is 2.5 g/cm³ for the volcanoes while it is 2.0 g/cm³ for Claritas, Coracis and Valles Marineris. The following parameters are held fixed in all models: mantle density $\rho_m = 3.5$ g/cm³, Young's modulus $E = 100$ GPa, Poisson's ratio $\nu = 0.25$. For 1D gravity analysis, the number of parameters of top/bottom models is reduced by 1) setting $T_c = 45$ km and $\rho_c = 2.9$ g/cm³, 2) taking increments of 0.1 g/cm³ for ρ_l and 20 km for T_e , 3) having maximum $T_c = 180$ km and maximum $f = 0.9$.

^bThe base varies in the following range (in km): (–1, 21) for Olympus, (3, 18) for Ascreaus, (6, 13) for Pavonis, (6, 18) for Arsia, (1, 6) for Alba, (2, 8) for Elysium, (3, 7) for Claritas and Coracis.

^cSee section 3.2.2: f' is related to F by $F = f'T_c/h_{\max}$, where h_{\max} is the topographic maximum inside the localizing window.

include both top and bottom loading. The top load is the topography which can have a density different from the crust density. Bottom loading can appear in various guises depending on the depth, spatial extension and sign of the underground density anomaly. In particular, the sign of the density anomaly defines two groups of models. In models of the first group, bottom loading compensates the top load in the isostatic sense, increasing mountain height and valley depth. This (positive) type of bottom loading can appear in the form of crustal thickening (resp. thinning) under a mountain (resp. valley), as a mantle plume under a volcano or as high density intrusions beneath a rift. In models of the second group, bottom loading decreases the amplitude of the topography due to top loading only. This (negative) type of bottom loading can appear under volcanoes as high density intrusions within the crust due to dikes, sills, and magma chambers. Bottom loading also occurs with random phase [Forsyth, 1985]. Uncorrelated bottom loading is however not easy to treat with localized spectral analysis because it does not result in a unique gravity signal which can be localized. In any case the correlation of the top and bottom loads is a reasonable assumption for isolated volcanoes and impact basins [Wieczorek, 2007].

[31] We construct two different models of bottom loading. In the first model, the bottom load is modeled as a relief at the Moho in phase with the initial top load. The amount of bottom loading is parameterized by the ratio f of the weight of the applied load at the Moho to the weight of the applied load on the surface [Forsyth, 1985]. The case $f > 0$ correspond to bottom loading of positive type, similar to the one used by McGovern *et al.* [2002] (the positive-type bottom loading of Belleguic *et al.* [2005] is set deeper in the mantle). In this model, we do not consider negative-type bottom loading because $f < 0$ may lead to a singular flexure equation. This indetermination results from the fact that the combined top and bottom loads (if f is not too close to zero) generate near-zero surface topography at some harmonic degree ℓ , so that the interface deflections cannot be computed in function of the surface topography (see Appendix A). At Valles Marineris, positive-type bottom loading causes crustal thinning so that the local crust thickness may become negative (e.g. if the crust thickness is small and the crust density is

high). Parameter values yielding such nonphysical models are rejected.

[32] In the second model, the bottom load is modeled as a density anomaly within the crust [Belleguic *et al.*, 2005] extending from the crust surface to a depth proportional to the topography. The depth (defined as positive) is bounded by the crust thickness and the density of the bottom load is taken to be equal to the top load density. The spatial extension of bottom loading is parameterized by the ratio F of the density anomaly depth to the topography. As this definition of the density anomaly is not compatible with negative topography, we only apply this model to targets having positive topography (large volcanoes and Thaumasia highlands). F varies between 0 and T_c/h_{\max} (in Table 3, the rescaled parameter f' varies between 0 and 1). In this model, bottom loading of negative type (positive density anomaly $\rho_l - \rho_c$) does not create singularities because there is no bottom load at degree ℓ if the topography vanishes at degree ℓ . For geophysical interpretation, we use instead of F the parameter f^* , defined as the ratio of the weight of the density anomaly to the weight of the topography:

$$f^* = \frac{\rho_c - \rho_l}{\rho_l} F, \quad (9)$$

which is positive (resp. negative) for bottom loading of positive (resp. negative) type. Flexure equations for our first model are those of McGovern *et al.* [2002] with $\rho_b = \rho_m - \rho_c$ (a small correction needs to be applied, see equation (A3)). Equations for our second model are derived in a similar way (here $\rho_b = \rho_c - \rho_l$) but equation B5 of McGovern *et al.* [2002] must be replaced by $F = -w_b/h_r$.

[33] In summary, models of the first kind, or *top/bottom models*, depend on 5 parameters: crust thickness T_c , crust density ρ_c , lithospheric elastic thickness T_e , load density ρ_l and bottom loading ratio f or f^* (see Table 3). Note that the crust thickness parameter refers to the planetary average value. Beneath large volcanoes, the crust is thicker than the average crust thickness because of lithospheric deflection; the gravity signal takes this effect into account through finite amplitude corrections. The mantle density, Young's modulus and Poisson's ratio are supposed to be known.

3.2.3. Top/Top Models

[34] We now propose a new kind of model addressing the question of loading history. If the load was emplaced at two different times, successive layers can have different densities. The elastic thickness of the lithosphere can also change between the two loading events.

[35] Regarding volcanoes, we would like to investigate whether the density of the volcanic shield is different from the density of the basement. In the case of the Tharsis Montes, the basement is the Tharsis rise which may have been emplaced long before the volcanoes themselves. We thus introduce a new density interface, called the *base*, between the reference surface underlying the volcano (see section 2.3) and its summit. There are two top loads with different densities, associated with two elastic thicknesses, and no bottom load. Since the flexure equation is linear, we compute the deflection due to each load before adding them.

[36] Regarding Valles Marineris, we would like to model the scenario proposed by *Andrews-Hanna* [2011] and *Davis and Andrews-Hanna* [2011]. In their model, Valles Marineris troughs formed in isostatic equilibrium with sedimentary filling which was later removed by erosion. The loading can thus be divided in two phases. In the later phase, the removal of sediments causes flexural uplift. In the earlier phase, the load is the topography (minus the flexural uplift) with Valles Marineris filled to the rim with sediments. Sediments and surrounding rock have different densities and each loading/unloading phase has its own elastic thickness. The sedimentary filling is modeled by the topography of Valles Marineris described in section 2.3, which is a correct approximation if flexural uplift has a small effect on the depth of the trough (measured with respect to the rims). If Valles Marineris is modeled as a line load, the maximum flexural uplift is at a distance $\pi\alpha$ from the load, with $\alpha^4 = 4ET_c^3/(12(1 - \nu^2)g\rho_m)$ [Turcotte and Schubert, 2002, p. 125]. The above approximation is thus valid if $\pi\alpha$ is much larger than the 5° half-width of the trough (Figure 3), that is if $T_c \gg 30$ km.

[37] The number of free parameters must be limited so that the computational time remains reasonable. *McGovern et al.* [2002, 2004b] and *Belleguic et al.* [2005] found out that the crust thickness T_c and crust density ρ_c are poorly constrained by admittance analysis, which can be understood by examining the parameter sensitivity of a simple model (see Appendix B). These parameters are thus held fixed at $T_c = 45$ km and $\rho_c = 2.9$ g/cm³ [Neumann et al., 2004, 2008]. As in top/bottom models, the mantle density, Young's modulus and Poisson's ratio are supposed to be known. Since the elastic thickness should increase with time, we impose that the elastic thickness associated with the upper load is larger than the one associated with the lower load.

[38] In summary, models of the second kind, or *top/top models*, depend on 5 parameters (for volcanoes): the base, two load densities, and two elastic thicknesses (see Table 3). For Valles Marineris, there is no base (the depth of sedimentary filling is fixed) so that there are only 4 parameters.

3.3. Parameter Estimation

3.3.1. Degrees of Freedom

[39] The number of free parameters in a model should be large enough so that the model can fit the data, but small enough otherwise parameters cannot be constrained. In spherical admittance analysis, it seems at first that the number of

degrees of freedom (hereafter d.o.f) is equal to the number of harmonic degrees used in the misfit range, that is 34 (resp. 52) for the 10° (resp. 15°) window. However, data windowing correlates admittance estimates in a range given by twice the taper bandwidth (see Appendix C) so that the number of strictly independent estimates is one (resp. two) for the 10° (resp. 15°) window. The number of equivalent d.o.f [Thomson and Chave, 1991; Percival and Walden, 1993] lies between these extremes. In the case of spectrum estimates from overlapping tapered series, the number of equivalent d.o.f saturates at twice the number of statistically independent estimates when the overlap becomes larger than 70% [Percival and Walden, 1993, p. 293]. On the basis of this analogy, let us suppose that there are two (resp. four) equivalent d.o.f for the 10° (resp. 15°) window. The majority of our models will thus have less equivalent d.o.f than free parameters.

[40] When fitting the admittance, we will see that having many free parameters does not ensure the existence of a good fit at all targets. One reason is that the range of each parameter is limited by physical considerations. Another is that flexure models have a non-linear dependence on their parameters, so that the set of relevant parameters can vary from one location to the other, depending on the relation between gravity and topography. Non-linearity is also introduced by finite amplitude computation of the gravity signal and by data tapering. This being said, it is well-known that admittance modeling often leads to multiple solutions because of the unavoidable trade-offs between parameters [McGovern et al., 2002]. For example, the elastic thickness typically decreases as the crust thickness increases because the compensating signal of the crustal root is attenuated. Also, the elastic thickness becomes irrelevant (isostasy) if there is positive-type bottom loading with $f = 1$ (see Appendix A). Compared to the load density, the density of the crust has less influence on the gravity signal because the contributions of upper and lower crust boundaries partly cancel (this is not true if bottom loading occurs as relief at the Moho). In top/top models, the two load densities and the base are highly correlated, so that the solution will usually be non-unique. In that case, we want to know whether a differentiated density structure can account for gravity data unexplainable otherwise. Finally, parameters whose value is unknown should not be fixed even if it makes it impossible to constrain other interesting parameters. In particular, estimates of the elastic thickness are not reliable if they depend on unjustified assumptions about the crust or load density.

3.3.2. Goodness-of-Fit

[41] The various nonlinearities (flexure model, finite amplitude gravity, tapering) of the localized spectral method make it impossible to invert the problem with linear least squares methods. In that case Bayesian inversion works better [Tarantola, 2005; Rivoldini et al., 2011], but it involves probability distributions that depend on unknown admittance covariances (see Appendix C). We will thus determine the best-fitting solutions through a grid search over discretized parameters (Table 3). An alternative would be to find the best-fitting solutions with the Marquardt method and determine ranges of acceptable solutions with Monte Carlo modeling [Phillips, 1994]. Genetic algorithms [Lawrence and Phillips, 2003] also shorten the search in parameter space but we did not try this method.

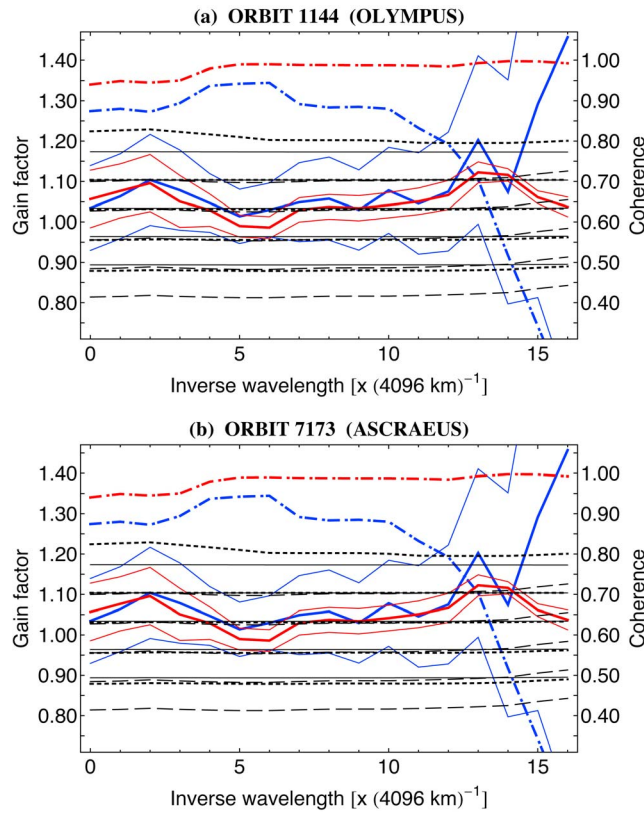


Figure 6. Spectral analysis of the acceleration residual ($\ell > 50$) for the pericenter passes of orbits 1144 and 7173: observed gain factors (thick curves), $\pm 1\sigma$ errors (thin curves), coherences (dash-dotted curves). MEX results are shown in blue while MRO results are shown in red. The predicted gain factor (black) varies in the range $\rho_t = 2.6 - 3.4 \text{ g/cm}^3$ (bottom to top) with an increment of 0.2 g/cm^3 . Predictions are shown for (1) $T_e = 80 \text{ km}$ and $f = 0$ (black horizontal lines), (2) $T_e = 40 \text{ km}$ and $f = 0$ (black dotted lines), (3) $T_e = 80 \text{ km}$ and $f = 0.5$ (black dashed lines).

[42] If gravity and topography are highly correlated, best-fitting models can be found by minimizing the RMS misfit M between observed and predicted admittances:

$$M^2 = \frac{1}{n} \sum_{i=i_1}^{i_2} \left(\frac{Z^{\text{obs}}(i) - Z^{\text{pred}}(i)}{\sigma_Z(i)} \right)^2, \quad (10)$$

where the index i denotes either the frequency or the harmonic degree (see section 3.1). The indices (i_1, i_2) define the range chosen for minimization and $n = i_2 - i_1 + 1$. The misfit depends on a correct estimate of the errors $\sigma_Z(i)$. We checked that the least squares errors given by equations (4) and (8) are generally close to those estimated with the jackknife method [Thomson and Chave, 1991], but jackknife errors can be larger by up to 50% at some frequencies or harmonic degrees.

[43] The minimization of M provides either preferred values for model parameters [McKenzie *et al.*, 2002] or acceptable ranges for them if a rejection threshold is chosen as in McGovern *et al.* [2002, 2004b]. The former approach

has the disadvantage that sets of parameters with very different values can lead to nearly the same misfit, so that preferred values may be far from the true values. Moreover the uncertainty on the parameters is not quantified in that approach. The choice of a rejection threshold for the misfit is an improvement in both respects, but the value of the threshold is somewhat arbitrary without a statistical interpretation (see Appendix C). In 2D analysis, we give ranges for the model parameters by rejecting values resulting in a RMS misfit larger than a given threshold ($M = 1$ or 2). In 1D analysis, we need to combine the estimates of the various profiles with weights taking into account the quality of the fit. These weights are usually given by the inverse squared error on the estimate. We cannot use a fixed threshold as in 2D analysis, otherwise the highest quality profiles would have the largest error. We thus assume that the error (up to a scale factor common to all profiles) is given by the parameter range such that the RMS misfit is smaller than some number (say 1.5) times the minimum misfit, as is common in the literature [McKenzie and Fairhead, 1997; Nimmo, 2002; Smrekar *et al.*, 2003].

[44] Though it is common practice, we do not study trade-offs between parameters with 2D contour plots of the misfit with respect to a pair of parameters. We think that these plots are not representative since they show only one slice of a 4- or 5-parameter space. Should the other parameters be fixed to reference values, or should they be set to their best-fit values? Besides, this approach is not appropriate for top/top models, where the misfit should at least be analyzed in a three-parameter space: ($h_b, \rho_{t1}, \rho_{t2}$) or (h_b, T_{e1}, T_{e2}). Instead, we will show the minimum misfit with respect to one parameter at a time.

[45] One should be very careful when interpreting the goodness-of-fit for top/top models because loading densities and elastic thicknesses are highly correlated with the base. In particular, the density below (resp. above) the base is weakly constrained when the base is close to its minimum (resp. maximum) value. The same is true for the elastic thicknesses. For example, reasonable fits can be found at Olympus Mons or at Claritas with small T_{e1} /large T_{e2} (when the base is low) or with large T_{e1} /small T_{e2} (when the base is high), but these small elastic thicknesses are not physically relevant (the physical constraint $T_{e1} \leq T_{e2}$ eliminates half of these solutions). It is thus advisable to reduce the number of free parameters (by setting $\rho_{t1} = \rho_{t2}$ or $T_{e1} = T_{e2}$) if the resulting model still yields good fits.

4. Results

4.1. Mars Express

4.1.1. Individual Profiles

[46] The first step consists in computing for each pericenter pass the coherence and gain factor (see section 3.1.2) between the acceleration residual (computed from the observed Doppler residuals) and the acceleration due to the uncompensated topography. The computation is done twice: once with the acceleration residual of MEX MaRS (hereafter abbreviated as MEX), and once with the acceleration residual predicted by the global gravity field MRO95A, hereafter noted MRO (see section 2.2). Below degree and order 50, this field has a negligible difference with the field JGM85F02 used by ESOC to reconstruct MEX orbit. Figure 6 illustrates

Table 4. Average Load Density (g/cm^3) From MEX and MRO Data^a

Target	$f = 0$		$f \neq 0$	
	ρ_{MEX}	ρ_{MRO}	ρ_{MEX}	ρ_{MRO}
Olympus	3.01 ± 0.29	3.07 ± 0.22	3.14 ± 0.26	3.21 ± 0.16
Ascræus	2.86 ± 0.15	2.99 ± 0.16	3.09 ± 0.19	3.20 ± 0.09
Valles Marineris	2.58 ± 0.10	2.60 ± 0.06	2.93 ± 0.23	2.95 ± 0.08

^aThe two models are without ($f = 0$) or with ($f \neq 0$) bottom loading (the elastic thickness is left free in both cases).

this spectral analysis for two different pericenter passes. In Figure 6a, errors on the MEX and MRO gain factors are comparable whereas the errors are much larger for MEX in Figure 6b because of a lower coherence.

[47] Next, we compute predictions for the gain factor with the top/bottom model (see section 3.2.2) depending on 3 parameters: the load density ρ_r , the elastic thickness T_e and the bottom loading ratio f (see Table 3 for parameter values). Predictions with more parameters become computationally intensive because the predicted gravity signal must be computed for each pericenter pass at every point of the trajectory. In any case, parameters such as the thickness and density of the crust have little impact at high degree (see Appendix B). Figure 6 shows predictions for varying load density in three different cases: no bottom loading with $T_e = 80$ km or 40 km, and with bottom loading ($f = 0.5$ and $T_e = 80$ km). The top loading model ($f = 0$) with a rather high elastic thickness ($T_e = 80$ km) predicts gain factors that are constant at all wavelengths, but whose value depends sensitively on the load density. The gain factor takes this simple form because the gravity signal is mainly due to the topography. The effect of the elastic thickness on the gain factor begins to show at $T_e = 40$ km (mostly at very high density) but is only significant at much smaller values of T_e (e.g. Valles Marineris with $T_e = 20$ km in Figure 9). The effect of bottom loading varies with the location. If the elastic thickness is 20 km or more and the bottom loading ratio is 0.4 or less, predictions at Olympus Mons only show small deviations with respect to the constant gain factor predicted by the top loading model with high elastic thickness (see Figure 6a). However, bottom loading significantly decreases the predicted gain factor at Ascræus Mons (see Figure 6b) and even more so at Valles Marineris (see Figure 9). Since the gain factor modified by bottom loading remains approximately constant over all wavelengths (at least if $\ell > 50$), the goodness-of-fit is not improved by the presence of bottom loading.

[48] Finally, we compute the misfit between the modeled and observed gain factors in the range of the 13 longest wavelengths and find the minimum misfit for each value of the load density. The preferred value of the load density corresponds to the overall minimum misfit, with uncertainties quantified by the range in which the misfit is less than 1.5 times the minimum misfit (after fitting a parabola to the function minimum misfit versus load density). As discussed in section 3.3.2, the threshold of 1.5 is arbitrary and the resulting uncertainty cannot be related to a confidence interval. However, it is useful as a weight when combining the estimates from different pericenter passes. Another choice of threshold approximately rescales all weights by the same

factor. After repeating this procedure for all pericenter passes above Olympus Mons, Ascræus Mons and Valles Marineris, we average over all estimates of the load density, using the uncertainties as weights (see Table 4). The uncertainty on the average estimate is given by the square root of the weighted variance [Bevington and Robinson, 2003].

[49] We draw the following conclusions:

[50] 1. If there is no bottom loading, the most likely values of the load density are highest ($3.0\text{--}3.1 \text{ g/cm}^3$) at Olympus Mons, a bit lower ($2.9\text{--}3.0 \text{ g/cm}^3$) at Ascræus Mons and lowest (2.6 g/cm^3) at Valles Marineris.

[51] 2. The presence of bottom loading favors higher density estimates: the shift is $0.1\text{--}0.2 \text{ g/cm}^3$ for Olympus, 0.2 g/cm^3 for Ascræus and about $0.3\text{--}0.4 \text{ g/cm}^3$ for Valles Marineris. However, the goodness-of-fit is not much improved by the presence of bottom loading.

[52] 3. For the volcanoes, MEX estimates are slightly lower than MRO estimates: about 0.06 g/cm^3 smaller for Olympus and about 0.12 g/cm^3 smaller for Ascræus; for Valles Marineris, the estimates are comparable.

[53] 4. MEX uncertainties are in most cases larger than MRO uncertainties, meaning that there is a larger dispersion of the different estimates. However, the fit between the observed gain factor and the predictions is not better with MRO than with MEX.

4.1.2. Spectral Average and Anisotropy

[54] The fit between models and observations (if $\ell > 50$) is not improved by bottom loading (see section 4.1.1). The elastic thickness T_e is not constrained and has little impact on the predictions unless T_e is close to zero, which is unlikely for the considered targets. If there is top loading only and if T_e is not close to zero, predictions of the gain factor (at high harmonic degrees) are independent of the precise location: the gain factor is a constant depending on the load density, varying by 10% if the load density varies by 10% (that is by 0.3 g/cm^3). In these conditions, it makes sense to compute the weighed average of the gain factors and the coherences associated with the pericenter passes for a given target because the predictions will be the same. An average reduces the uncertainty of the gain factor and allows us to check whether the spectral dependence of the data is in agreement with the models. The left panels of Figures 7, 8, and 9 show the average gain factor at Olympus Mons, Ascræus Mons and Valles Marineris (Middle West section only) for the residual gravity signal at cut off at degree $\ell = 50$. The right panels of the same figures show the gain factor for the gravity signal cut off at degree $\ell = 30$. Only three pericenter passes (orbits 2061, 2072, 2105) in the Middle West section of Valles Marineris are taken into account because of their higher quality and to average over a limited area. We draw the following conclusions:

[55] 1. At Olympus Mons, the gain factor is not constant: at the cutoff $\ell = 50$, the dominant characteristic is a decrease from long to short wavelengths. The MEX gain factor disagrees at very long wavelengths but the coherence is also lower. At the lower cutoff $\ell = 30$, both gain factors increase from long to short wavelengths (there is also a decrease at wavelengths smaller than 400 km which agrees with what is seen at the cutoff $\ell = 50$). These results are explained below by the presence of anisotropy.

[56] 2. At Ascræus Mons and Valles Marineris, the gain factor for the cutoff $\ell = 50$ is compatible with constant

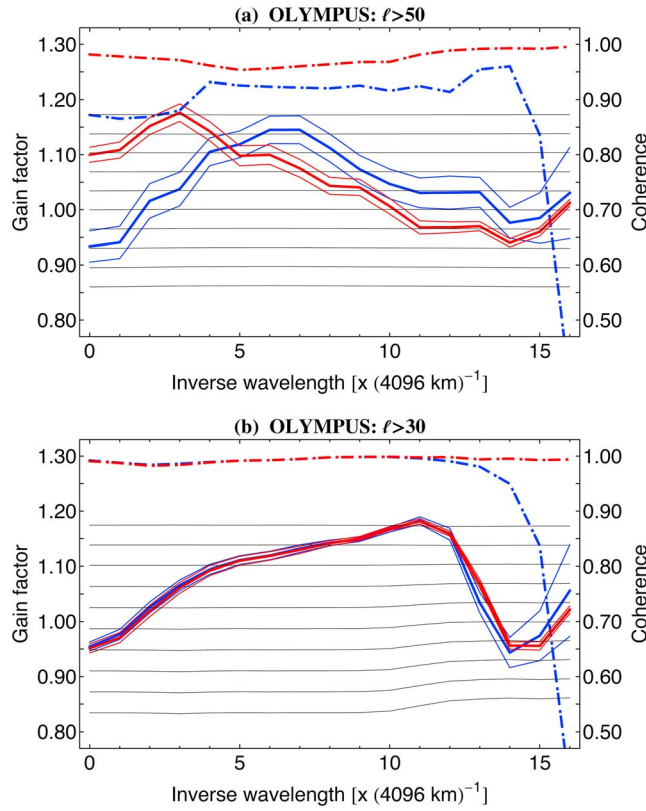


Figure 7. Average gain factor and coherence at Olympus Mons at two different cutoffs: (a) $\ell > 50$; (b) $\ell > 30$. Colored curves refer to observed gain factors (thick curves), $\pm 1\sigma$ errors (thin curves), coherences (dash-dotted curves). MEX results are shown in blue while MRO results are shown in red. The predicted gain factor (black horizontal lines) varies in the range $\rho_t = 2.5 - 3.4 \text{ g/cm}^3$ (bottom to top) with an increment of 0.1 g/cm^3 ($T_e = 80 \text{ km}$ and $f = 0$).

predictions in the range where the coherence is very high. The inferred load density is consistent to the results of the analysis of individual pericenter passes (see Table 4).

[57] 3. At Ascraeus Mons and Valles Marineris, the gain factors for the cutoff $\ell = 30$ are higher and lower than for the cutoff $\ell = 50$, respectively. The gain factor at Ascraeus Mons decreases from long to short wavelengths, which is explained below by the presence of anisotropy. For Valles Marineris, the discrepancy is explained by bottom loading which shifts the predictions differently at each cutoff. Observed gain factors are compatible at the two cutoff values with models having the values of Table 4 ($f \neq 0$). For Ascraeus Mons, the estimate of the load density varies with the scale of analysis (fixed here by the cutoff): there is a large structure with high density and a smaller structure (400 km wavelength) of smaller density.

[58] The gain factor at Olympus Mons ($\ell > 50$ and $\ell > 30$) and at Ascraeus Mons ($\ell > 30$) is not constant. It is true that predicted gain factors are not constant if one rejects the assumptions of top loading only and large elastic thickness (see Figures 6a and 9). However the resulting wavelength dependence does not decrease from long to short wavelengths as seen in Figures 7a and 8b. As discussed at the

end of section 3.1.2, the wavelengths appearing in the 1D spectral analysis are not only affected by the size of the gravity perturbations but also by the orientation of the associated wave vectors. For example, the gain factor at long wavelengths is mainly caused by the sectoral coefficients (harmonic order m close to harmonic degree ℓ) of the gravity field. If the cutoff is at $\ell = 50$ (resp. 30), 1D wavelengths longer than 420 km (resp. 700 km) are mainly due to sectoral coefficients. The decrease (resp. increase) of the gain factor from long to short wavelengths thus means that sectoral coefficients of the gravity signal give rise to a higher (resp. smaller) gain factor than zonal coefficients.

[59] We check this hypothesis by computing the anisotropic 2D localized admittance (see section 3.1.3) between the global gravity field and the planetary shape modified by finite amplitude corrections (these corrections are included so that the admittance is closer in definition to the 1D gain factor). Figure 10 shows that the usual ‘isotropic’ 2D admittance computed from all harmonic coefficients of degree and order (ℓ, m) is neither identical to the dominantly zonal admittance (computed with the constraint $m \leq \ell/2$), nor to the dominantly sectoral admittance (computed with the constraint $m > \ell/2$). At Olympus Mons, the dominantly sectoral admittance is higher than the dominantly zonal admittance for harmonic degrees $\ell > 50$ whereas the converse is true in the range $30 < \ell < 50$. This result is in agreement with the admittance decrease seen in Figure 7a (discarding the admittance drop at very long wavelength in

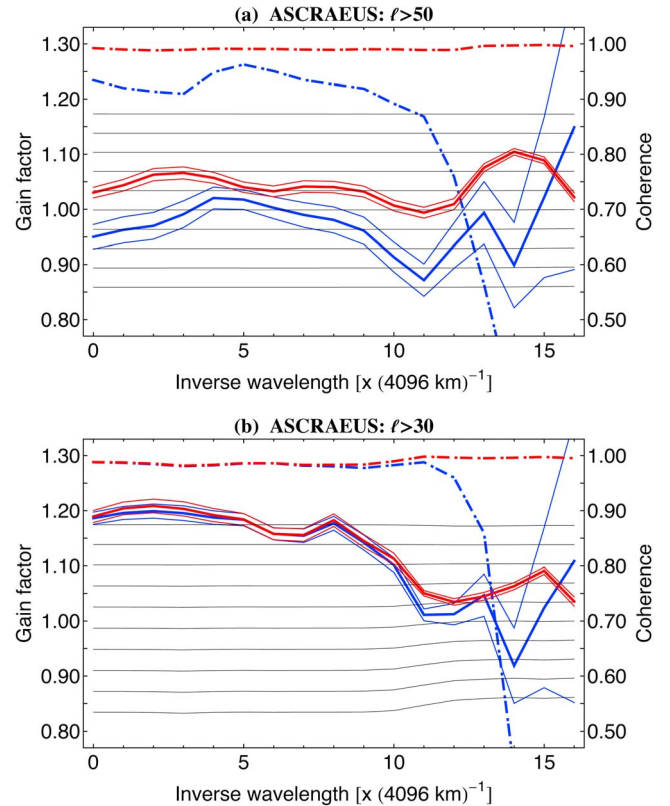


Figure 8. Average gain factor and coherence at Ascraeus Mons at two different cutoffs: (a) $\ell > 50$; (b) $\ell > 30$. Curves are identified as in Figure 7.

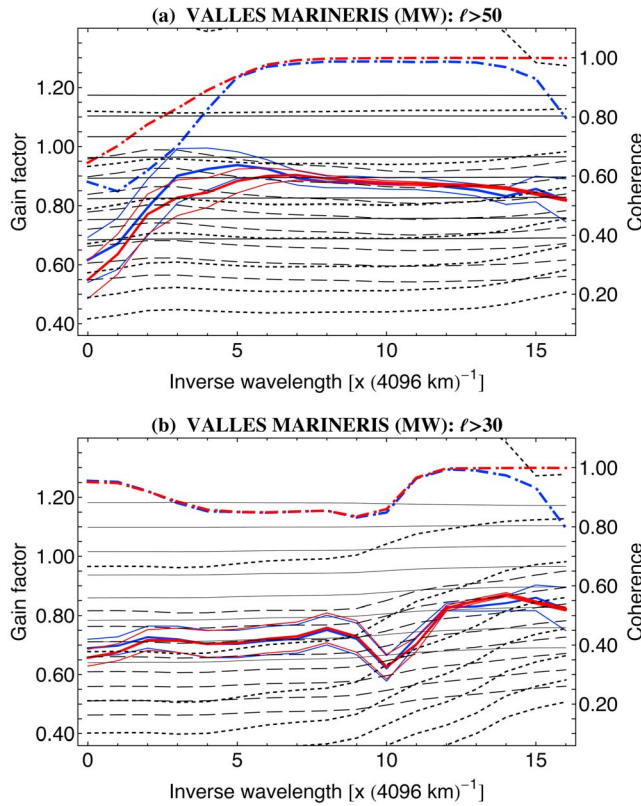


Figure 9. Average gain factor and coherence at the Middle West part of Valles Marineris at two different cutoffs: (a) $\ell > 50$; (b) $\ell > 30$. Curves are identified as in Figure 7, except for the predictions. The predicted gain factor (black) varies in the range $\rho_t = 2.0 - 3.4 \text{ g/cm}^3$ (bottom to top), the increment being 0.2 g/cm^3 (twice the increment in Figures 7–8). Predictions are shown for (1) $T_e = 80 \text{ km}$ and $f = 0$ (black horizontal lines), (2) $T_e = 20 \text{ km}$ and $f = 0$ (black dotted lines), (3) $T_e = 80 \text{ km}$ and $f = 0.5$ (black dashed lines).

MEX data) and the increase in admittance seen in Figure 7b (discarding the admittance drop at very short wavelength seen in both MEX and MRO data). At Ascraeus Mons, the dominantly zonal admittance is lower than the dominantly sectoral admittance in the range $30 < \ell < 50$ whereas dominantly zonal and dominantly sectoral admittances are nearly identical for degrees $\ell > 50$. This in agreement with the approximately constant admittance seen in Figure 8a and with the admittance decrease seen in Figure 8b. The anisotropy of the global gravity field is further discussed in section 4.2.3.

4.2. Mars Reconnaissance Orbiter

4.2.1. Model Specifications

[60] The gravity signal is predicted with three types of models (section 3.2) depending on 5 (or less) free parameters: top/bottom models with bottom loading at the Moho (TB0) or within the crust (TB0*), and top/top models with two load densities and two elastic thicknesses (TT0). The notation n in TT n refers to the number of additional constraints. Top/bottom models with four and three parameters

are obtained by setting bottom loading to zero (TB1, with $TB1^* = TB1$) and by setting the crust thickness and density to reference values (TB2 and TB2*), respectively. Top/top models have only four parameters if load densities are equal (TT1a) or if elastic thicknesses are equal (TT1b). At Valles Marineris, the base is fixed so that Models TT0 and TT1a-b depend on four and three free parameters, respectively. The constraints on the various models are compared in Table 5.

[61] As a benchmark, we tested whether our top/bottom models reproduce the results that *Belleguic et al.* [2005] obtained for the volcanoes with another gravity field (MGS85H2) at the limited resolution of $\ell_{\text{resol}} \approx 65$. Assuming the same resolution (thus a restricted misfit range), we computed marginal probabilities for the load density, elastic thickness and bottom loading ratio with the formula $P \sim \exp(-M^2/2)$ (criticized in Appendix C). We found a good match between our results and their Figures 6, 7 and 10 showing marginal probabilities for the load density, elastic thickness and bottom loading ratio (note that the uncertainties quoted by *Belleguic et al.* [2005] in their Table 3 are 1σ for the elastic thickness but 2σ for the load density).

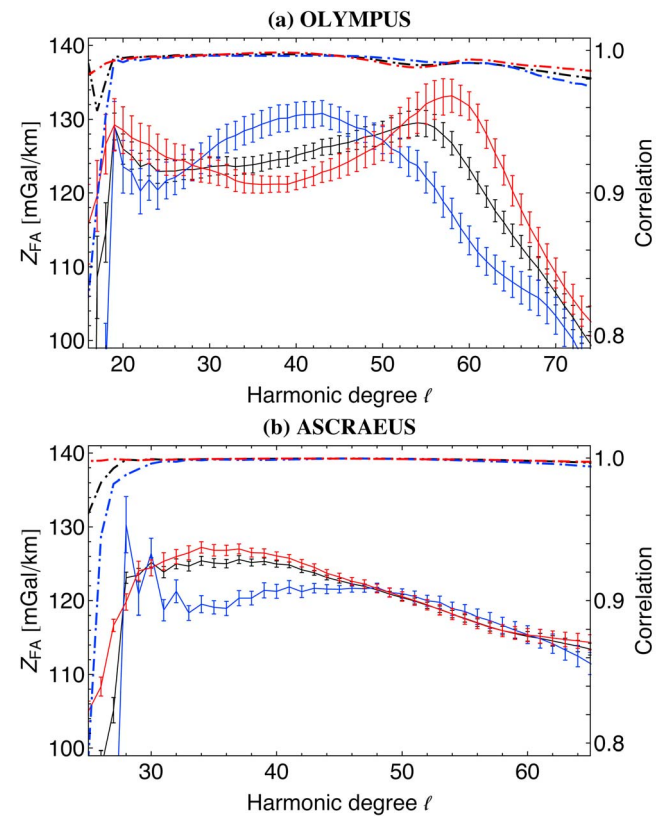


Figure 10. Anisotropy of the 2D localized admittance Z_{FA} between the global gravity field MRO110B and the planetary shape modified by finite amplitude (FA) corrections. The targets are (a) Olympus Mons and (b) Ascraeus Mons. The curves with error bars show the 'isotropic' admittance from all harmonic coefficients (in black), the dominantly zonal admittance from coefficients of harmonic order $m \leq \ell/2$ (in blue), and the dominantly sectoral admittance from coefficients of harmonic order $m > \ell/2$ (in red). The associated correlations are drawn as dash-dotted curves.

Table 5. Characteristics of Top/Bottom and Top/Top Models

Model	p	Constraints ^a					Misfit Range ^b		
		$T_c = T_{c0}$	$\rho_c = \rho_{c0}$	$f, f^* = 0$	$\rho_{t1} = \rho_{t2}$	$T_{e1} = T_{e2}$	$\ell_{win} = 6$	$\ell_{win} = 16$	$\ell_{win} = 25$
TB0, TB0*	5				✓	✓			
TB1	4			✓	✓	✓	(13,74)	(23,74)	(32,65)
TB2, TB2*	3	✓	✓		✓	✓			
TT0	5	✓	✓	✓					
TT1a	4	✓	✓	✓	✓		(9,74)	(19,74)	(28,65)
TT1b	4	✓	✓	✓		✓			

^aAt Valles Marineris, the base is always fixed so that p , the number of free parameters, should be replaced by $p - 1$ in top/top models. The reference values for the crust thickness and density are as in Table 3 ($T_{c0} = 45$ km, $\rho_{c0} = 2.9$ g/cm³) except that $T_{c0} = 50$ km in Model TB2 so that it corresponds to one of the discrete values used in Model TB0.

^bThe misfit range indicates which harmonic degrees are used for the computation of the misfit, with the inferior bound given by $\ell_1 = \ell_{win} + 3$ or $\ell_{win} + 7$ and the superior bound by $\ell_2 = \ell_{resol} - \ell_{win}$, with $\ell_{resol} = 90$ (see section 3.1.3). The large window used for the analysis of all Valles Marineris is set to $\ell_2 = 74$ since Figure 13 shows that the gravity fields MRO110B and MRO110B2 diverge beyond this degree.

4.2.2. Goodness-of-Fit

[62] The observed admittance is fitted at each target with the various models of section 4.2.1. The minimum misfits (Table 6) indicate whether a model is acceptable ($M \leq 1$ in Thaumasia highlands, $M \leq 2$ elsewhere) and whether the fit is better or worse when switching to another model. Figures 11, 12, and 13 show the observed correlation and admittance, as well as the best fitting models TB0 and TT0.

[63] The top/bottom model without bottom loading (TB1) does not fit the data ($M > 2$) at Pavonis Mons, Alba Mons and VM-Far West, while the misfit at Olympus Mons, VM-Middle West and VM-Far East is barely under threshold. The addition of bottom loading at the Moho (TB0) significantly improves the fit at Olympus Mons (where it increases the predicted admittance for $\ell < 30$) and at VM-Middle West (where it decreases the predicted admittance for $30 < \ell < 50$). Positive-type bottom loading also reproduces the drop in admittance at Claritas for $55 < \ell < 76$, though the impact on the goodness-of-fit is negligible. Bottom loading within the crust (TB0*) may occur at Ascraeus, Pavonis, Arsia and Elysium Montes but it does not significantly improve the fit except at Ascraeus Mons. Setting the crust thickness and density to their reference values (TB2) increases the misfit at all volcanoes, resulting in an acceptable fit at only two volcanoes out of six (also true if one applies similar constraints to Model TB0*). The inclusion of low degrees ($\ell_{win} + 3 \leq \ell \leq \ell_{win} + 6$) significantly degrades the best fit at Olympus and Elysium Montes (changing the TB1 minimum misfit from 1.9 to 2.4 at Olympus and from 1.3 to 2.1 at Elysium).

[64] Top/top models perform as well as or better than top/bottom models at all targets except Elysium Mons, especially if the misfit range includes the low degrees associated with the Tharsis bulge. In spite of significant improvement in goodness-of-fit, top/top models do not fit well the data at Pavonis Mons, Alba Mons, and VM-Far East, while they fail at VM-Far West.

[65] At each target, we estimate model parameters by selecting one top/bottom model and one top/top model giving an acceptable fit with the least number of parameters. The models selected for the volcanoes are TB1 and TT1b, unless the minimum misfit is very close to the threshold $M = 2$, in which case TB1 is replaced by TB0 (Olympus) and TT1b is replaced by TT0 (Pavonis, Alba, Elysium). Note that TB2 fits Arsia and Elysium Montes with only three parameters but the fitting range is small: $\rho_t \geq 3.35$ g/cm³, $T_e = 20 - 40$ km,

$f = 0.1 - 0.2$ at Arsia Mons and $\rho_t \geq 3.4$ g/cm³, $T_e = 20$ km, $f = 0.1$ at Elysium Mons. In Thaumasia highlands, the 3-parameter model TB2 fits the data with or without bottom loading (top/top models give similar results and are omitted). In Valles Marineris, the selected models are the 3-parameter models TB2 and TT1a (the latter is chosen because the load density ρ_{t2} cannot be constrained in Models TT0 and TT1b). Tables 7–8 give ranges for model parameters such that the misfit is less than $M = 2$ (reduced to $M = 1$ at Thaumasia highlands because of the good fit). Since the threshold value is somewhat arbitrary, Figures 14, 15, and 16 show the curves of minimum misfit for several models when model parameters are varied. The parameter values minimizing the overall misfit can also be read from these curves.

4.2.3. Global Gravity Field: Spectral Dips and Anisotropy

[66] In their exhaustive paper on the gravity field MRO110B, Konopliv *et al.* [2011] state that simple flexural models cannot match the spectral dips that occur at high degree in the admittance at Olympus and Elysium Montes. Actually, the spectral dips at these two volcanoes are of different nature, since the admittance first drops at Olympus Mons beyond $\ell = 56$ while the correlation remains high (above 0.9), and then drops again beyond $\ell = 85$ (together with the correlation). At Elysium Mons, the admittance and correlation drop together beyond $\ell = 73$ (see Figure 11). The first admittance dip at Olympus Mons is thus real, while

Table 6. Minimum Misfit for Top/Bottom and Top/Top Models^a

Target	Top/Bottom Models				Top/Top Models		
	TB0	TB0*	TB1	TB2	TT0	TT1a	TT1b
Olympus	1.3	1.8	1.9	2.3	1.1	2.2	1.1
Ascraeus	1.0	0.4	1.0	3.4	0.5	3.1	0.9
Pavonis	2.5	2.3	2.6	2.9	1.6	3.3	1.9
Arsia	0.4	0.7	0.7	1.0	0.4	3.8	0.6
Alba	3.3	3.0	3.3	4.1	1.9	3.9	2.0
Elysium	1.1	1.1	1.3	1.5	1.5	3.0	2.0
Claritas	0.4	0.5	0.6	0.6	0.5	0.6	0.5
Coracis	0.6	0.6	0.6	0.7	0.8	0.9	0.8
VM (FW)	3.8	-	3.8	3.9	2.8	2.8	3.9
VM (MW)	1.1	-	1.9	1.2	0.9	1.6	2.4
VM (ME)	1.2	-	1.2	1.3	1.1	1.2	1.3
VM (FE)	1.6	-	1.8	1.8	1.4	1.4	1.7
VM (Global)	0.8	-	1.1	0.9	0.8	0.9	1.3

^aModel specifications are given in Table 5 (Model TB2* is omitted here). Misfits in boldface are larger than the threshold $M = 2$.

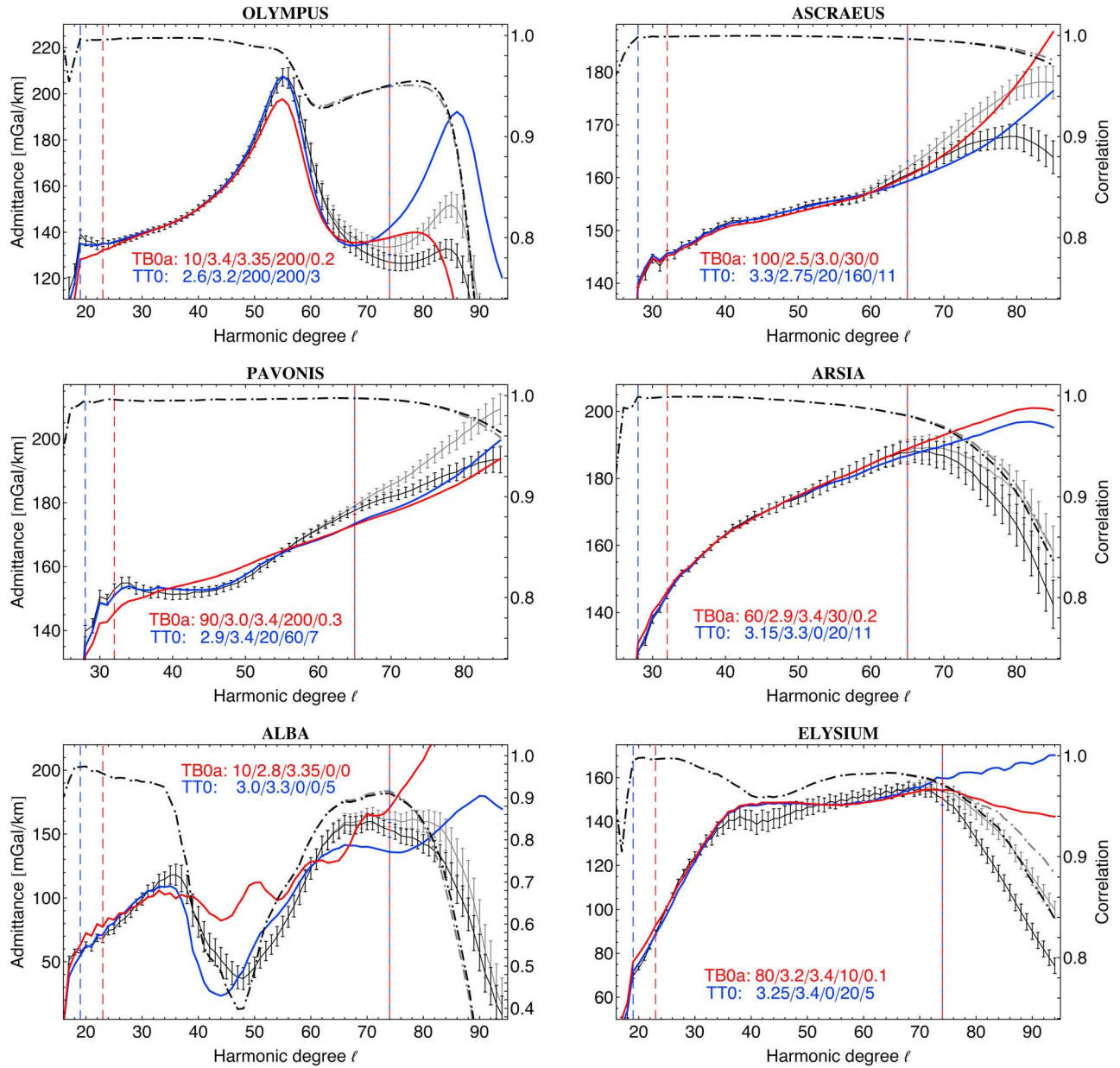


Figure 11. Admittance (solid curves) and correlation (dash-dotted curves) at the volcanoes. The observed admittance and correlation are shown for the gravity field MRO110B (black) and MRO110B2 (gray). Error bars correspond to the 1σ uncertainty in the admittance (see equation (8)). Admittance and correlation from the best-fitting models TB0 (red) and TT0 (blue). Best-fitting parameter values are given as $T_c/\rho_c/\rho_t/T_e/f$ (TB0) and as $\rho_{t1}/\rho_{t2}/T_{e1}/T_{e2}/h_b$ (TT0) with the units of Table 3. Vertical dashed lines (blue and red) indicate the misfit range for each model.

the second one as well as the one at Elysium Mons are due to the lack of resolution. Our top/bottom and top/top models both reproduce the admittance dip at Olympus Mons, as shown in Figure 11. Spectral peaks occurring before the spectral dips are due to finite amplitude corrections computed at the reference altitude which is lower than the volcano elevation. The admittance becomes much flatter if it is computed either at a higher altitude, or with respect to the shape including finite amplitude corrections, as seen by comparing Figures 10 and 11.

[67] Konopliv *et al.* [2011] also conclude that the admittance is better estimated with only the 10 nearest sectoral coefficients: they claim that the correlation is improved beyond $\ell = 12$ and that the spectral dip disappears (see their Figure 14). We agree that the better determination of the near-sectoral coefficients - due to the polar orbit of the spacecraft - generally leads to a higher correlation beyond $\ell = 70 - 80$. However, Figure 17a shows that the first spectral dip at Olympus Mons is present not only in the estimate of the admittance made with the 10 nearest zonal coefficients (Z_{10}^{zonal}), but also in the one made with the 10

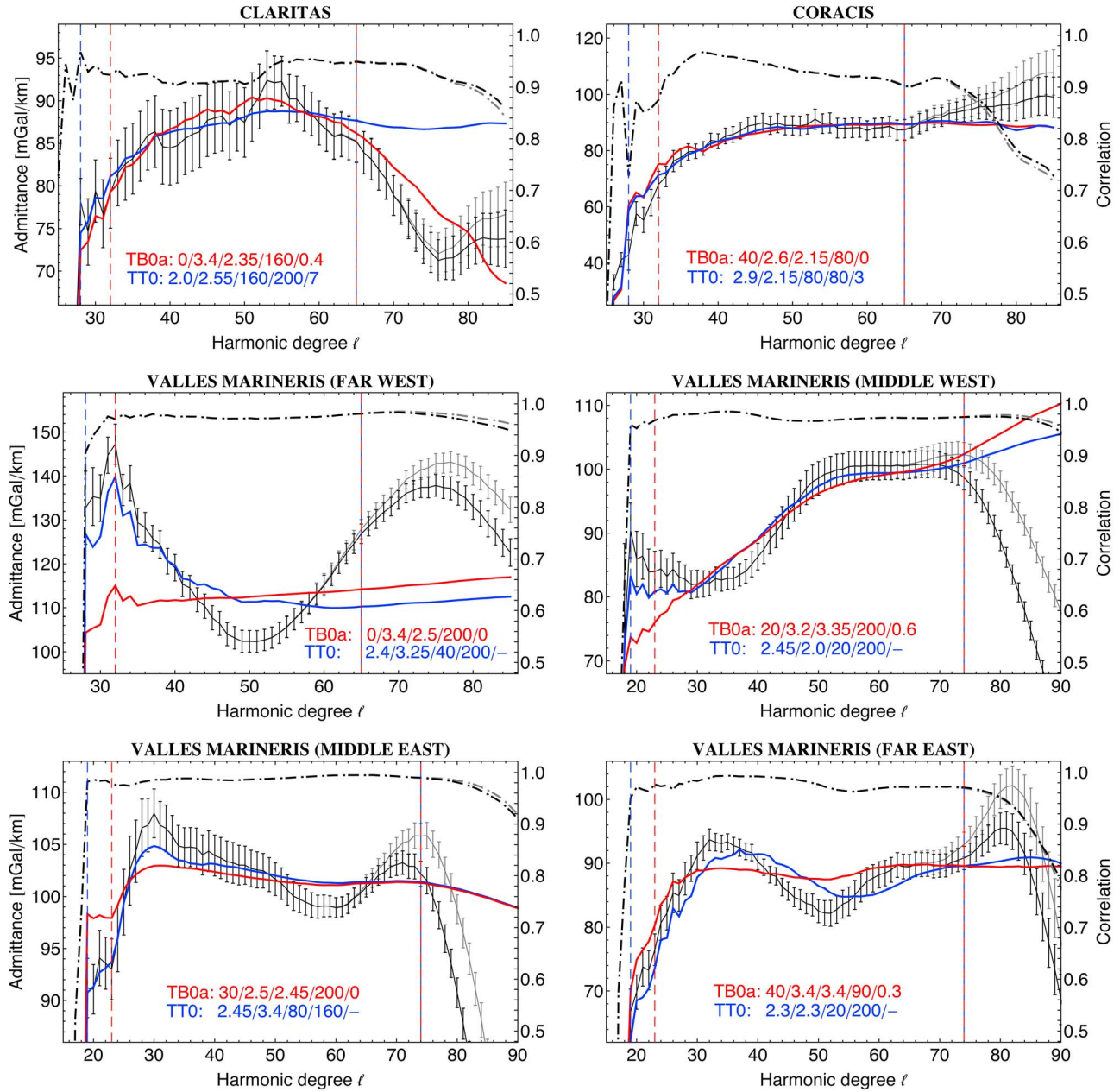


Figure 12. Admittance and correlation in the Thaumasia highlands and in Valles Marineris (see Figure 11 for details).

nearest sectoral coefficients (Z_{10}^{sect}). Besides, the near-sectoral and near-zonal correlations are extremely close up to $\ell = 55$ and remain high (above 0.9) up to $\ell = 84$. Since the near-zonal and near-sectoral admittances are both of good quality in the misfit range, the polar orbit of the spacecraft cannot explain their difference.

[68] The admittance anisotropy can be measured with the misfit (see equation (10)) between Z_{10}^{sect} and the isotropic admittance Z_{10}^{obs} . The errors $\sigma_{\mathcal{A}(i)}$ are those on Z_{10}^{sect} (the factor 2ℓ in equation (8) should be set to 20) and the misfit range is the same as in top/bottom models. By rotating the planet (anticlockwise) around Olympus Mons, we can check that the misfit is maximum with no rotation and minimum for a 45° rotation (Figure 17b). We could also define a misfit

with Z_{10}^{zonal} , but Z_{10}^{sect} remains closer to Z_{10}^{obs} under rotations because windows close to the equator have more power in sectoral than in zonal coefficients. While the misfit is also maximum without rotation at Arsia Mons, the maximum misfit is reached at Ascraeus, Pavonis, Alba and Elysium Montes for rotations of 70° , 30° , 20° and 60° , respectively. The anisotropy is thus not always maximum in the latitude/longitude coordinate frame, which is another argument against explaining the anisotropy with the polar orbit geometry. The minimum/maximum values of the misfit are 0.8/1.9, 0.8/3.1, 0.4/5.0, 0.6/3.1, 1.8/7.9 and 1.0/2.6 for Olympus, Ascraeus, Pavonis, Arsia, Alba and Elysium Montes, respectively. The anisotropy is particularly large at Pavonis and Alba Montes and could be one of the reasons

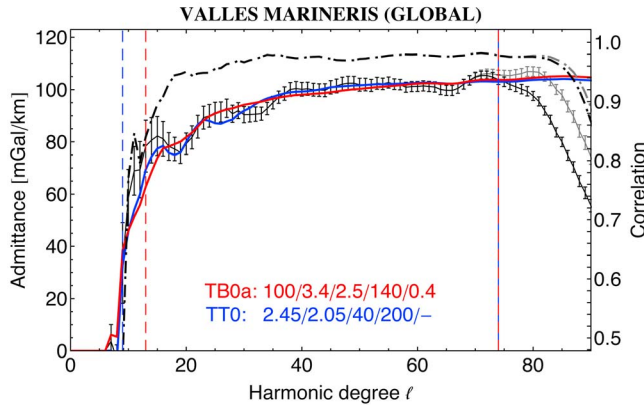


Figure 13. Admittance and correlation in Valles Marineris with a global window (see Figure 11 for details).

why top/bottom and top/top models fail to give good fits at these two targets. In conclusion, near-sectoral and near-zonal terms contribute differently to the admittance because of the intrinsic anisotropy of the admittance, as already discussed with MEX data in section 4.1.2.

[69] Mechanical models of the lithosphere are usually isotropic, in the sense that the relation between gravity and topography in the spectral domain is independent of the harmonic order m [Bills and Lemoine, 1995]. Existing anisotropic models assume that the elastic thickness differs according to the direction [Simons *et al.*, 2000; Swain and Kirby, 2003; Kirby and Swain, 2006; Audet *et al.*, 2007; Audet and Mareschal, 2007]. Since the elastic thickness has a smaller impact than the surface density at high harmonic degrees, we attribute the anisotropy to horizontal variations of density. Variations of several tenths of g/cm^3 are required to explain the misfit differences between near-zonal and near-sectoral admittances. Horizontal variations of density are thus probably of the same order of magnitude as the vertical density variations appearing in top/top models.

Table 7. Constraints on the Parameters of Selected Top/Bottom Models^a

Target	Model	T_e (km)	ρ_c (g/cm^3)	ρ_t (g/cm^3)	T_e (km)	f
Olympus	TB0	≤ 70	<i>n.c.</i>	≥ 3.25	≥ 110	≤ 0.2
Ascraeus	TB1	≥ 40	≤ 2.6	$3.0-3.1$	$20-60$	-
Pavonis	<i>no fit</i>	-	-	-	-	-
Arsia	TB1	≥ 50	≤ 2.9	$3.0-3.2$	≤ 10	-
Alba	<i>no fit</i>	-	-	-	-	-
Elysium	TB1	<i>n.c.</i>	<i>n.c.</i>	≥ 2.95	≤ 30	-
Claritas	TB2	-	-	≤ 2.35	≥ 90	≤ 0.4
Coracis	TB2	-	-	≤ 2.65	≥ 70	≤ 0.6
VM (FW)	<i>no fit</i>	-	-	-	-	-
VM (MW)	TB2	-	-	$2.40-3.15$	≥ 80	$0.1-0.7$
VM (ME)	TB2	-	-	$2.4-2.55$	≥ 110	≤ 0.1
VM (FE)	TB2	-	-	$2.15-2.45$	≥ 120	≤ 0.2
VM (Global)	TB2	-	-	$2.35-3.10$	≥ 70	≤ 0.6

^aRanges are determined from Figures 14-15-16 so that the misfit M is under threshold: $M \leq 1$ for Claritas and Coracis, $M \leq 2$ for the volcanoes and Valles Marineris; *n.c.* means 'no constraint'.

Table 8. Constraints on the Parameters of Selected Top/Top Models^a

Target	Model	ρ_{t1} (g/cm^3)	ρ_{t2} (g/cm^3)	T_{e1} (km)	T_{e2} (km)	h_b (km)
Olympus	TT1b	≤ 3.1	≥ 3.15	≥ 80	-	$0-15$
Ascraeus	TT1b	≥ 3.25	≤ 3.05	≥ 20	-	$7-15$
Pavonis	TT0	$2.8-3.1$	3.4	≤ 40	$60-120$	$7-9$
Arsia	TT1b	≤ 3.2	≥ 3.2	≤ 80	-	$7-15$
Alba	TT0	$3.00-3.05$	3.3	0	0	5
Elysium	TT0	3.25	≥ 3.35	0	20	$3-5$
VM (FW)	<i>no fit</i>	-	-	-	-	-
VM (MW)	TT1a	$2.25-2.40$	-	≤ 20	≥ 140	-
VM (ME)	TT1a	$2.4-2.5$	-	≥ 20	≥ 100	-
VM (FE)	TT1a	$2.15-2.35$	-	≥ 20	≥ 100	-
VM (Global)	TT1a	$2.3-2.6$	-	≤ 180	≥ 80	-

^aMisfit thresholds are as in Table 7. Results for Claritas and Coracis are omitted because good fits require layers of nearly equal density and rather large elastic thicknesses, as in Model TB1. At Valles Marineris, models having small values of T_{e2} are rejected (see section 3.2.3).

[70] Giving up the isotropy assumption poses the problem of inverting data for models having a large number of parameters. Alternatively, we could constrain the non-uniform density from the observation of anisotropic features. As a first example, the large aprons at the northeast and southwest flanks of the three Tharsis Montes [Plescia, 2004] could be of different density than the main edifices. As a second example, high-density crustal intrusions beneath the volcanoes could be continuous from Arsia Mons in the southwest to Ascraeus Mons in the northeast, creating bottom loading oriented in the northeast-southwest direction. A more systematic study of the sources of anisotropy could be conducted by (1) identifying the direction of maximum isotropy, (2) rotating the coordinate system around the target so as to align this direction with the north-south axis, (3) computing the near-zonal and near-sectoral admittances, (4) dividing the spectral range into subsets in which the difference between the anisotropic admittances is either positive or negative, (5) constructing the topography corresponding to these subsets, (6) trying to associate this partial topography with observed features.

5. Discussion

5.1. Composition of Rocks

5.1.1. Tharsis Rise

[71] On the basis of orbital remote-sensing data, the in-situ analysis by rovers and the composition of Martian meteorites, Mars is now seen as a basalt-covered world [McSween *et al.*, 2009; Ross Taylor and McLennan, 2008]. However, it remains possible that a more ancient andesitic (lighter than basalt) crust underlies the basaltic cover [Nimmo and Tanaka, 2005], although the only robust evidence in favor of this hypothesis consists of rock analyses by Mars Pathfinder [McSween *et al.*, 2009]. Remote-sensing data gives little information specific to Tharsis. A major problem is the thick dust mantle covering most of the province, making it impossible to derive the rock mineralogy with the Thermal Emission Spectrometer (TES) aboard Mars Global Surveyor. Lang *et al.* [2009] however found relatively dust-free lava flows south of Arsia Mons for which they could determine a basaltic composition having affinities with Martian

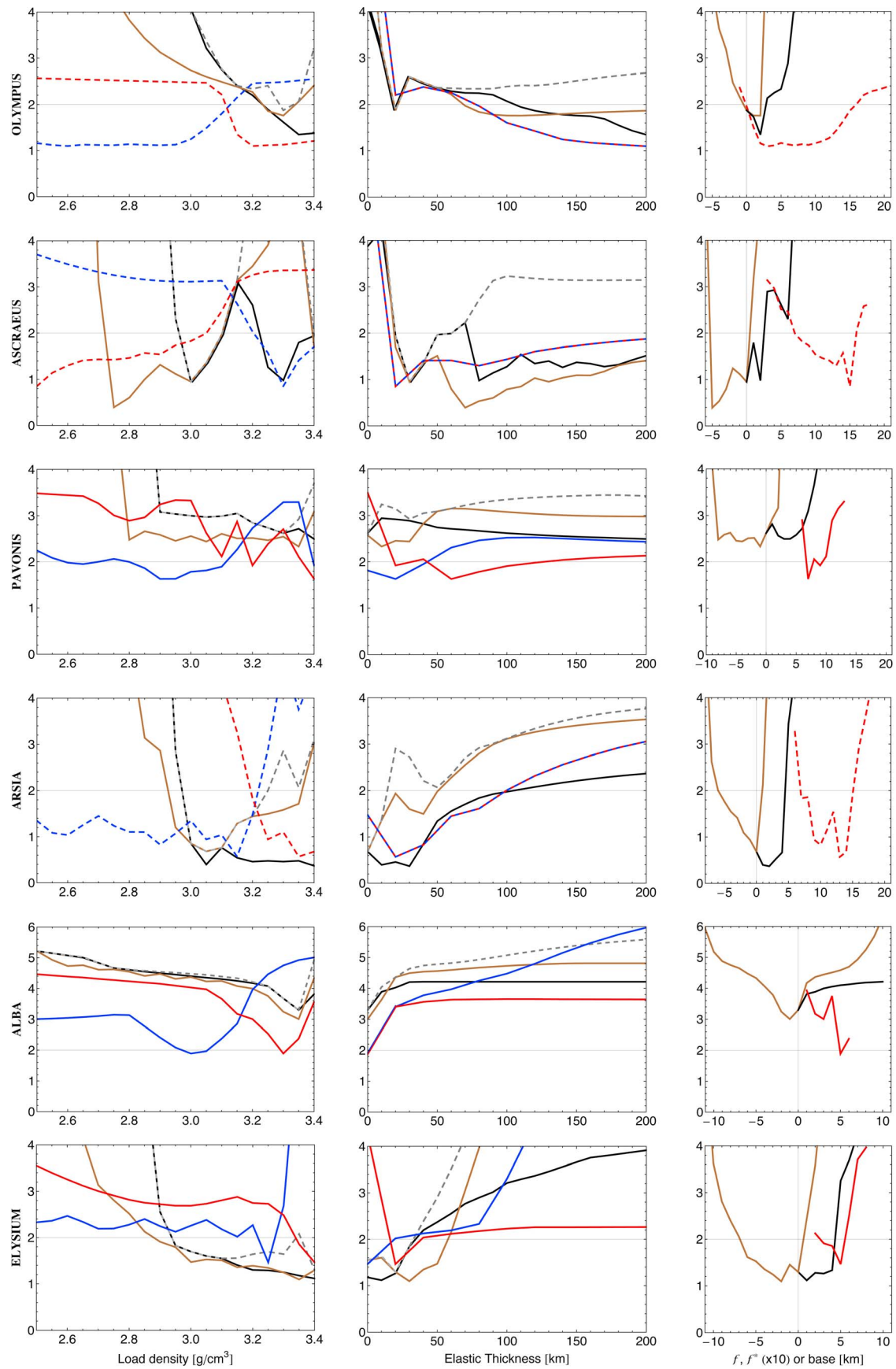


Figure 14

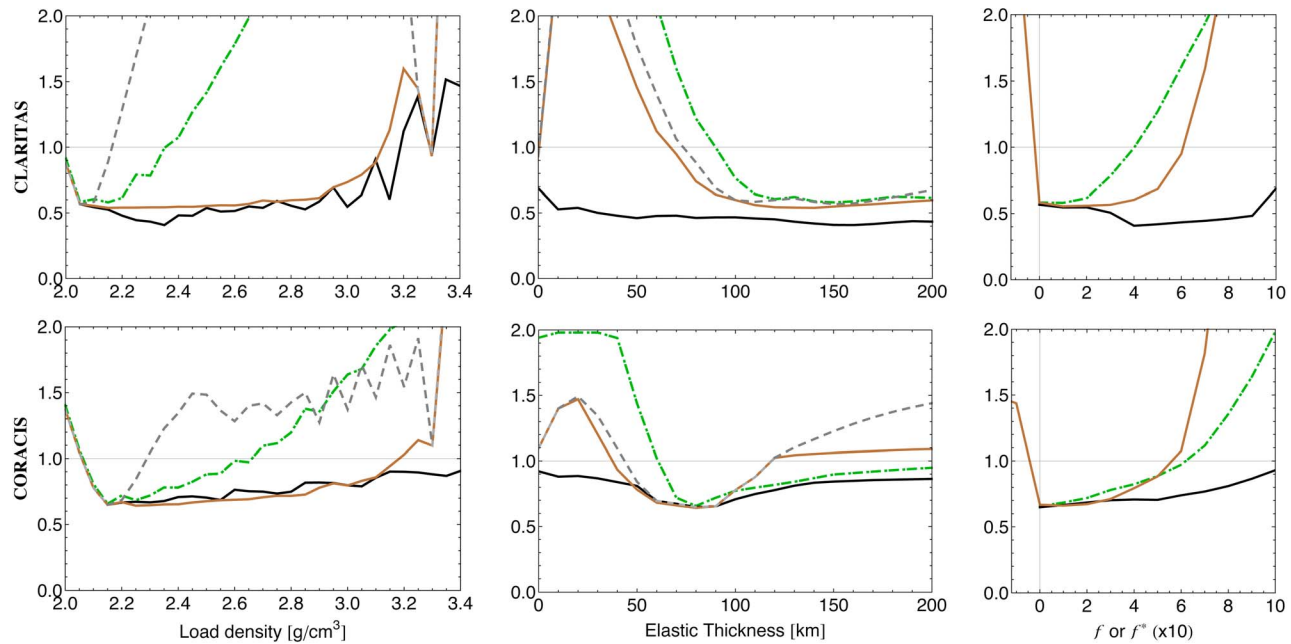


Figure 15. Thaumasia highlands (Claritas and Coracis): minimum misfit in selected top/bottom models. Colors distinguish between Models TB0 (black), TB0* (brown), TB1 (gray), and TB2 (green). Continuous curves refer to 5-parameter models (TB0, TB0* and TT0), dashed curves refer to 4-parameter models (TB1) and dot-dashed curves refer to 3-parameter models (TB2).

meteorites (shergottites). Dust mantling is less of a problem for the Gamma Ray Spectrometer (GRS) aboard Mars Odyssey because its penetration depth is a few tens of centimeters, much more than the few tens of μm with TES. GRS revealed a depletion of silica and an enrichment in chlorine in the western part of Tharsis (including the Tharsis Montes and Olympus Mons) [Boynton *et al.*, 2007]; the chemical composition of this area is compatible with undifferentiated magmas originating in the Martian mantle at a depth of 125–170 km [El Maarry *et al.*, 2009]. Beside the evidence from remote sensing, morphometric analysis of lava flows also point to a basaltic/andesitic composition of young lava flows on Ascræus Mons [Hiesinger *et al.*, 2007], and to a basaltic composition of the plains surrounding the Tharsis Montes [Hauber *et al.*, 2011]. Martian meteorites probably provide the best evidence for the composition of Tharsis, because their young crystallization ages suggest they come from young volcanic terrains on Tharsis or maybe Elysium [McSween, 2002]. Unfortunately the dust blanket precludes nearly everywhere the identification by spectroscopic analysis of possible sources of meteorites [Hamilton *et al.*, 2003; Lang *et al.*, 2009]. Some Martian meteorites (such as basaltic shergottites) are extrusive basalts and have a pore-free density of about 3.31 g/cm^3 , similar to lunar basalts, whereas other meteorites have an ultramafic composition with a pore-free density between 3.4 and 3.7 g/cm^3 [Neumann *et al.*, 2004; Macke *et al.*, 2011]. In comparison, the computed

pore-free density of the Mars Pathfinder soil-free rock is only 3.06 g/cm^3 [Neumann *et al.*, 2004].

5.1.2. Valles Marineris

[72] Valles Marineris (VM) was originally thought to be cut into a megaregolith layer [Lucchitta *et al.*, 1992], which could account for the low density found with admittance analysis. However the wall rocks do not appear to be brecciated by impacts [McEwen *et al.*, 1999]. Pictures reveal that canyon walls are composed down to the bottom of layers a few tens of meters thick, which have been interpreted either as flood basalts [McEwen *et al.*, 1999], or as intrusive basaltic magmas [Williams *et al.*, 2003], or as lacustrine sediments [Malin and Edgett, 2000]. TES measurements identify the surface mineralogy in the eastern part of VM as being mainly basaltic [McSween *et al.*, 2003]. In the Far Eastern part of VM (see Table 2), the combination of TES and THEMIS (Thermal Emission Imaging System aboard Mars Odyssey) data give evidence for a thin basaltic layer of huge horizontal extent ($1100 \text{ km} \sim 18^\circ$) [Christensen *et al.*, 2003; Edwards *et al.*, 2008]. In the Middle Eastern part of VM, stratigraphic analysis of canyon walls indicates that thin strong layers (probably lava flows) alternate with thick weak layers (maybe volcanic tephra or sediments) [Beyer and McEwen, 2005]. Thus the density of the cliff rocks sensitively depends on the unknown degree of compactification of the weak layers. High-resolution images and spectra from MRO have (not yet) revealed sedimentary layers in the

Figure 14. Large volcanoes: minimum misfit in selected top/bottom and top/top models. Colors distinguish between Models TB0 (black), TB0* (brown), TB1 (gray), and TT0 or TT1b (blue for ρ_{t1} and T_{e1} ; red for ρ_{t2} , T_{e2} and h_b). Continuous curves refer to 5-parameter models (TB0, TB0* and TT0) whereas dashed curves refer to 4-parameter models (TB1 and TT1b). The bottom loading ratio f^* is defined by equation (9). Misfits are drawn as continuous distributions but are actually discrete.

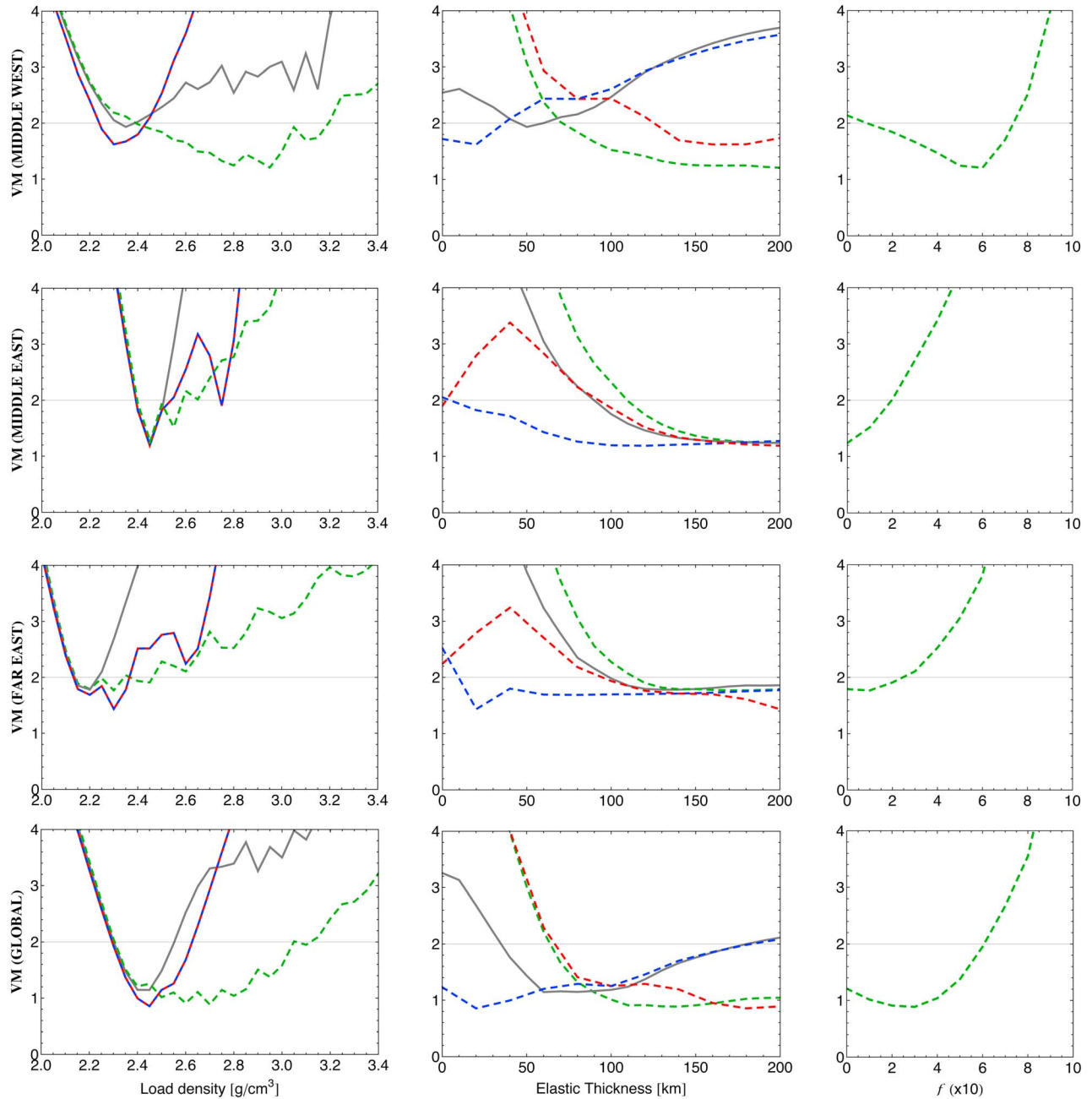


Figure 16. Valles Marineris: minimum misfit in selected top/bottom and top/top models. The Far West section of Valles Marineris is not shown since no model fits it well. Colors distinguish between Models TB2 (green), TB1 (gray), and TT1a (blue for ρ_{t1} ; red for ρ_{t2} , and h_b ; blue/red for $T_{e1} = T_{e2}$). The base being fixed, continuous curves refer to 4-parameter models (TB1) whereas dashed curves refer to 3-parameter models (TB2 and TT1a).

canyon walls of VM [Flahaut *et al.*, 2012], showing rather dense mafic dikes intruding the walls of eastern Coprates Chasma [Flahaut *et al.*, 2011]. In eastern VM, the lower portion of the walls seems to consist of pristine Noachian crust differing in composition from the Hesperian-aged lavas of western VM [Flahaut *et al.*, 2012].

5.2. Admittance Analyses at Larger Scale

[73] Local admittance analyses only became possible when Mars Global Surveyor improved our knowledge of the

Martian gravity field (see section 2.2). The first admittance studies localized this data set with very large windows. McKenzie *et al.* [2002] modeled line-of-sight MGS data above the Tharsis bulge with a top loading model, estimating the density to be 2.99 g/cm^3 and the elastic thickness to be 70 km. Lowry and Zhong [2003] chose to minimize the correlation between surface and internal loads in the Tharsis province; they obtained a density of 2.6 g/cm^3 and an elastic thickness of 110 km. Since the topographic power (and the gravity power) of Tharsis is dominated in the range

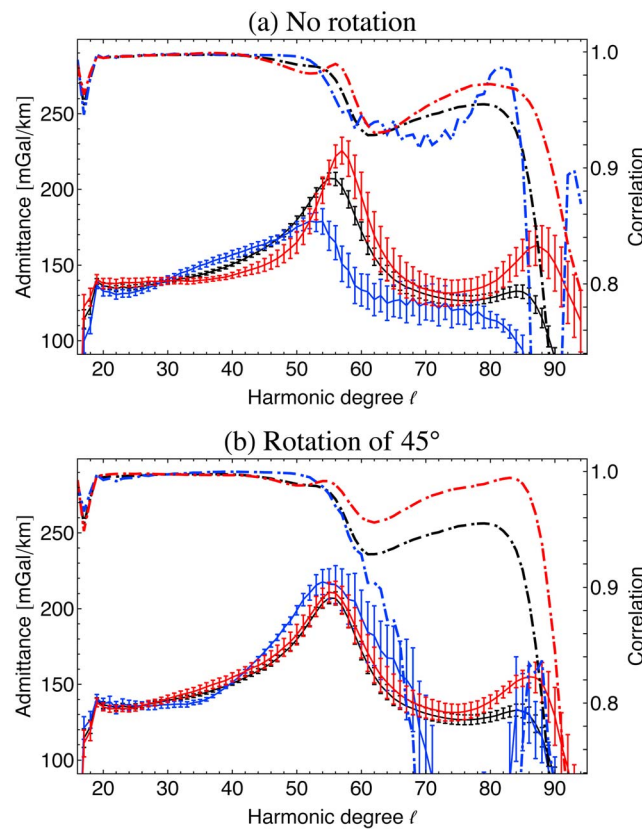


Figure 17. Anisotropic admittance and correlation at Olympus Mons (a) without rotation and (b) after a 45° rotation of the planet around Olympus Mons. Solid (resp. dash-dotted) curves show the admittance (resp. correlation) between the global gravity field MRO10B and the planetary shape. Colors distinguish between the admittance (or correlation) computed with all harmonic coefficients (Z^{obs} , in black), with only the 10 nearest zonal coefficients of the localized fields (Z^{zonal}_{10} , in blue), and with only the 10 nearest sectoral coefficients of the localized fields (Z^{sect}_{10} , in red).

$\ell = 10 - 70$ by the large volcanoes (see Figure 4), these estimates represent a weighed average of the values at each volcano and are not much affected by the rest of Tharsis. More recently, Williams *et al.* [2008] separated Tharsis into a western region, containing the large volcanoes, and a southeastern region, containing the Thaumasia highlands as well as Valles Marineris. Their best fit for the density and elastic thickness is (3.15 g/cm^3 , 81 km) for west Tharsis (with nearly no bottom loading) and (2.25 g/cm^3 , 162 km) for southeast Tharsis (with an important contribution from incoherent bottom loading). Again, these estimates for west Tharsis correspond to an average over the large volcanoes, whereas the estimates in southeast Tharsis mainly depend on Valles Marineris, the power of which dominates the contribution of the Thaumasia highlands (see Figure 4a).

5.3. Large Volcanoes

5.3.1. Age

[74] Admittance analysis yields estimates of the lithospheric thickness at the time of loading, which can then be converted into heat flux estimates. It is thus interesting to

know when the load was emplaced in order to test scenarios of thermal evolution [Hauck and Phillips, 2002; Schumacher and Breuer, 2006a, 2006b; Guest and Smrekar, 2007; Grott and Breuer, 2008, 2010]. In general, we expect to find a smaller lithospheric thickness for older features (the surface heat flux was then larger) but this trend can be hidden by spatial variations of the heat flux. On the basis of stratigraphy and crater counting, the Martian history is divided into three main periods: first the Noachian, then the Hesperian starting 3.5–3.7 Ga ago and finally the Amazonian starting 2.9–3.3 Ga ago [Hartmann and Neukum, 2001; Hartmann, 2005; Werner and Tanaka, 2011].

[75] Looking for a correlation age/heat flux, McGovern *et al.* [2002] and [Grott and Breuer 2008, 2010] classified the Tharsis Montes and Olympus Mons in the youngest period, the Amazonian, whereas Alba and Elysium Montes were set in the Amazonian-Hesperian period. Volcanic calderas in the Tharsis province were indeed active until 100–250 Ma ago [Werner, 2009; Robbins *et al.*, 2011], whereas the volcanic activity at Elysium Mons already stopped 2.8–3.1 Ga ago. From crater counting on volcano flanks, Werner [2009] however concludes that the main shield formation of the Tharsis and Elysium Montes ended about 3.5–3.6 Ga ago. Neukum *et al.* [2004] and Neukum *et al.* [2010] found similar ages for a few areas on the flanks of Olympus, Ascraeus and Arsia Montes, without concluding that these ages correspond to the main construction phase. The flank surface of Olympus Mons is a few hundred million years [Werner, 2009], but the main construction phase seems to have occurred between 3.67 Ga and 3.53 Ga ago [Jozwiak *et al.*, 2011]. The beginning of the activity is constrained by the age of a lava flow not following the down-slope of the surrounding trough while the end of the main building phase is given by the age of aureole deposits due to mass failure of the mountain flanks [Hiller *et al.*, 1982]. Moreover comparison with eruption rates of Hawaiian volcanoes suggest that large Martian volcanoes could have formed in a few tens of millions of years [Plescia, 2004]. Regarding their main construction phase, the three Tharsis Montes and Olympus Mons could thus belong to the Hesperian period, in which case they cannot serve as an indicator of the lithospheric thickness (or heat flux) in the Amazonian period. There is however no consensus on the pre-Amazonian history of the large volcanoes: for example, Hiesinger *et al.* [2007] date the Ascraeus shield to at least 1–1.5 Ga. Various studies suggest a trend in the surface age of the Tharsis Montes, with the latest activity either at Ascraeus Mons [e.g., Bleacher *et al.*, 2007] or at Arsia Mons [Robbins *et al.*, 2011], but these analyses do not tell us when the main shields were constructed.

[76] Morphologic analysis [Plescia, 2004; Ivanov and Head, 2006] and crater counting [Werner, 2009; Robbins *et al.*, 2011] indicate that Alba Mons was built in several stages on a long period of time, from 3–3.5 Ga to 200–300 Ma ago. The slow construction of Alba Mons is probably the reason why it is so difficult to model its gravity signal with simple mechanical models of the lithosphere.

5.3.2. Density and Lithospheric Thickness

[77] To make a long story short, the most robust conclusion is that at least some part of the load is of high density (above 3.2 g/cm^3) at all volcanoes. Quantitative estimates are however model-dependent. Before discussing the modeling problem, we note that the short-wavelength ($\ell > 50$)

MEX MaRS data yield densities lower by $0.1 - 0.2 \text{ g/cm}^3$ than estimates with the global gravity field, but the estimates are compatible within the error bars.

[78] Top/bottom models work well without bottom loading (TB1) at Ascraeus and Arsia Montes, and reasonably well at Elysium Mons (Table 6), predicting load densities larger than 2.95 g/cm^3 (see Table 7). Bottom loading only marginally improves the fit at Arsia and Elysium Montes, contrary to what was found by *Belleguic et al.* [2005]. The main effect of buoyant bottom loading at the Moho (TB0) is to favor higher load densities. Buoyant bottom loading within the crust (TB0* with $f^* > 0$) does not improve the fit at any volcano. At Ascraeus Mons, high density crustal intrusions (TB0* with $f^* < 0$) significantly improve the already good fit. At Olympus Mons, bottom loading at the Moho ($f = 0.2$) combined with very small crust thickness (10 km), high density crust (3.4 g/cm^3) and load (3.35 g/cm^3) lead to a better fit, though not good enough to confirm the validity of Model TB0 especially since the values of parameters are so extreme. The resulting crustal thickening of more than 100 km (due to the small density contrast between crust and mantle) could signal the presence of a mantle plume. Top/bottom models are not adequate at Pavonis and Alba Montes. Overall, bottom loading does not seem to be essential for the modeling of volcanoes, at least in the form taken in TB0 and TB0*. The elastic thickness must be large at Olympus Mons ($\geq 110 \text{ km}$) and is small at Ascraeus (20–60 km), Arsia ($\leq 10 \text{ km}$) and Elysium Montes ($\leq 30 \text{ km}$), though larger values are possible at Ascraeus and Arsia Montes in the presence of bottom loading. At Olympus Mons and Ascraeus Mons, top/bottom models require extreme values for the crust thickness T_c and density ρ_c . Arsia Mons is the only volcano where top/bottom models provide a very good fit with the crustal parameters fixed to their reference values (Model TB2 in Table 6), with the surprising result (already noted in *Belleguic et al.* [2005]) that the favored elastic thickness is small compared to what is required at Olympus Mons.

[79] Top/top models perform as well or better at all volcanoes, except Elysium, without requiring extreme values for T_c and ρ_c (see Table 6). The best fit at Pavonis and Alba is however not good enough; a better model still needs to be found for these two volcanoes. The relatively poor fit at Elysium is mainly due to the difficulty of fitting the low degrees that are not taken into account in top/bottom models (see section 4.2.2). As in top/bottom models, the elastic thickness is large at Olympus Mons ($\geq 80 \text{ km}$) whereas small values are favored at Pavonis (T_{e1}), Alba and Elysium Montes. At Ascraeus and Arsia Montes, the elastic thickness is not as well constrained but Figure 14 shows that the best fits are obtained with $T_e < 40 \text{ km}$ (Ascraeus) and $T_e < 60 \text{ km}$ (Arsia). Regarding the density structure, Olympus, Pavonis, Arsia, Alba and Elysium Montes have an upper top load of high density (larger than 3.15 g/cm^3 for Olympus and even larger for the other ones) and a lower top load of lower density, though the base is weakly constrained at Olympus and Arsia Montes. The density of the lower top load is poorly constrained at most volcanoes but it is lower than the upper top load density, except at Ascraeus Mons. At Ascraeus Mons, top/top models suggest that the volcano has an inverse density structure, with lower density in the upper top load. This interpretation is supported by the MEX MaRS

data above Ascraeus Mons, which yields high densities at long wavelengths ($\ell > 30$) and lower densities at short wavelength ($\ell > 50$).

[80] We emphasize that the base is not equivalent to the height at which density changes. The base is rather the volcano height at the end of the first loading phase, which is later deflected by the upper top load. This later deflection is only a few kilometers at Olympus (T_{e2} is large) and Ascraeus (ρ_{t2} is not very high) Montes, but can reach tens of km at other volcanoes because of the high density of the upper top load and the small elastic thickness during the second loading phase. The whole shields of Arsia, Pavonis, Alba and Elysium Montes are thus of high density (even though the base is not close to the reference surface except at Pavonis), as is the main part of Olympus and Ascraeus shields. Our conclusion thus broadly confirms the high load density determined by *Belleguic et al.* [2005] and *McGovern et al.* [2004b] with lower resolution data for all large volcanoes. The high density of large volcanoes estimated with admittance analysis is compatible with the basaltic composition of Tharsis as determined by remote-sensing and agrees with the measured density of Martian meteorites if porosity is negligible within the volcanoes (see section 5.1).

5.3.3. Two Interpretations

[81] The initial hypothesis behind top/top models was that the volcanic shields of Tharsis Montes and Alba Mons formed as high density loads on a basement of lower density (the older Tharsis rise). Top/top models do not support this scenario because good fits are only obtained with a base significantly above the reference surface of each volcano. We now give two possible interpretations of the results of top/top models.

[82] In the first scenario, the density of the extruded lava changed from low (andesitic) to high (basaltic) during the construction of all large volcanoes, except at Ascraeus where the construction directly began with high density lava. If the large volcanoes mainly formed in the Hesperian (see below), this change of lava type possibly coincided with the transition from explosive to effusive eruption style that occurred 3.5 Ga ago [*Robbins et al.*, 2011]. Among the three Tharsis Montes, the switch from low density to high density occurs at the highest altitude at Arsia, closer to the reference surface at Pavonis and at zero altitude (under the reference surface) at Ascraeus Mons. This trend could indicate that Arsia and Pavonis Montes were respectively the first and second volcanoes to appear whereas Ascraeus Mons was the last one, at a time when the switch from low to high density lava was over. At Ascraeus Mons, the density of the extruded lava decreased at a later stage, which is compatible with the basaltic to andesitic composition of the young lava flows determined by *Hiesinger et al.* [2007].

[83] One problem with the first scenario is to explain why the lava type would change during the construction of the main shield. Another problem is that the elastic thickness is large at Olympus Mons during the emplacement of the high density load, whereas it is favored to be small or very small at the other volcanoes. Small elastic thicknesses are compatible with the 30 km value that *Grott and Breuer* [2010] predict for a Hesperian-aged Tharsis feature (Solis Planum) with a thermal evolution model. Olympus Mons thus appears to be in a class of its own, with a very large elastic thickness, while smaller elastic thicknesses are favored at

other large volcanoes. *Comer et al.* [1985] already reached this conclusion from tectonic analysis [see also *Solomon and Head*, 1990], but their small values for the elastic thickness at the Tharsis Montes were criticized by *McGovern et al.* [2002], who rejected their interpretation of grabens surrounding the volcanoes as being due to flexural stresses. The initially high elastic thicknesses in *McGovern et al.* [2002] were however corrected to lower values in *McGovern et al.* [2004b]. A later formation of Olympus Mons (during the Amazonian) would be consistent with a large elastic thickness, but this explanation seems excluded by the Hesperian age of the aureole deposits. Though the Olympus Mons was smaller than its present size when aureole deposits formed, the basal scarp resulting from the flank failure [*McGovern et al.*, 2004a] is about 6 km high, implying that the volcano already reached heights of more than 6–7 km 3.5 Ga ago [*Neukum et al.*, 2004]. If the main edifices of Olympus and the Tharsis Montes were emplaced at the same time, one must conclude that the elastic thickness had great spatial variations during the Hesperian, presumably due to mantle plumes [*Solomon and Head*, 1990; *Kiefer and Li*, 2009; *Grott and Breuer*, 2010], or to crustal thickening under Tharsis [*Schumacher and Breuer*, 2007; *Grott and Breuer*, 2010].

[84] In the second scenario, the presence of high density material below the reference surface of the volcano is not necessarily associated with lithospheric flexure. In our flexure models, the lithosphere under all volcanoes except Olympus Mons undergoes large deflections due to the high density load acting on a weak lithosphere. These deflections are also very localized because the elastic thickness is small and the base is rather high (in the limit of zero elastic thickness, deflection only occurs within the footprint of the load). In the case of Arsia Mons, the 13 km base (best-fit for TT1) is deflected by 24 km. Since the elastic thickness is only 20 km, the deflected surface is not much larger than the cross-section of the volcano at 13 km height, with a radius of about 140 km (the caldera is 130 km across and the edifice width is about 430 km according to [*Plescia* 2004]). The very localized nature of the high density root suggests that it originates in high-density igneous intrusions (magma chamber included) which solidify and are supported by a very rigid lithosphere. All volcanoes would be underlain by the same rigid lithosphere supporting Olympus Mons. If this interpretation is correct, the small elastic thickness found with our flexure models is not real and only serves to reproduce the observed density structure. This hypothesis gains some support from the good fits obtained with Model TB0* (high-density crustal intrusions) at Ascraeus, Arsia and Elysium Montes, although the elastic thickness is not much larger than in Model TB0. We thus need to develop new models in which igneous intrusions have a much smaller horizontal extension than in TB0*. The absence of a deep root of high density at Olympus Mons could be explained by a magma chamber within the volcano itself, as proposed by *Zuber and Mouginis-Mark* [1992] on the basis of tectonic analysis. Similarly, *Kiefer* [2004] proposed that extinct magma chambers account for the large gravity anomalies detected at highland volcanoes such as Syrtis Major [see also *Kiefer and Lillis*, 2011; *Grott and Wiczeorek*, 2011]. The second scenario suffers however from a major weakness: a large elastic thickness is incompatible with the Hesperian age of the main shields.

[85] Our admittance analysis does not confirm the central values that *Belleguic et al.* [2005] obtained for the elastic thickness at the various volcanoes. The wide range of elastic thicknesses obtained with various models shows that this geophysically crucial parameter remains very uncertain even with high resolution gravity data. This problem has two causes. First the dependence of the gravity signal on the elastic thickness decreases at finer scales, so that the influence of the elastic thickness on the misfit gets smaller as the maximum harmonic degree increases. Second, the admittance cannot be fitted at all volcanoes with a 3-parameter model such as TB2 or with a 4-parameter top loading model such as TB1. Thus one needs a more complex description of the density distribution, either as some kind of bottom loading (possibly in the form of very localized high-density crustal intrusions), or in the form of a differentiated top load. The drawback is that it becomes more difficult to constrain the elastic thickness.

[86] Finally, the admittance anisotropy found in 1D and 2D analyses makes it clear that our isotropic models fail to fully describe the data. Though the elastic thickness can depend on the direction, it is most likely that the anisotropy is caused by spatial variations of the load density.

5.4. Thaumasia Highlands

[87] Simple top loading models (such as Model TB1) work well in the Thaumasia highlands, but they require a very small load density ($\rho_t < 2.15 - 2.25 \text{ g/cm}^3$, see Figure 15). The misfit has also a local minimum at $\rho_t = 3.3 \text{ g/cm}^3$ but the corresponding values of the elastic thickness and crust density are extreme ($T_e = 0 \text{ km}$ and $\rho_c = 3.4 \text{ g/cm}^3$). Higher densities closer to the reference crustal density are allowed if there is positive-type bottom loading at the Moho or within the crust (as low-density intrusions). Negative-type bottom loading (high-density crustal intrusions) is not present. Top/top models give similar results because layers of differing density and/or elastic thickness do not significantly improve the fit. The elastic thickness is weakly constrained in all models, being larger than 90 km and 70 km (Model TB2) at Claritas and at Coracis, respectively.

[88] Let us compare these constraints with previous results. On the one hand, the elastic thickness was estimated with topographic modeling. *Grott et al.* [2005] applied a flexural model to 1D profiles across the eastern Coracis Fossae Rift (34.5°S, 274.5°E) and obtained an elastic thickness of 10–12 km. *Grott et al.* [2007] modeled the depth of faulting of two lobate scarps in the southern Thaumasia region (40–44°S, 261–268°E) and estimated it to be in the range 21–35 km (the elastic thickness should be smaller but close to this value). On the other hand, the loading density and the elastic thickness have been estimated with spatial analysis of 1D acceleration profiles. *Williams et al.* [2008] fitted line-of-sight acceleration profiles of the Mars Global Surveyor spacecraft above the Thaumasia highlands (between 22°S and 50°S), using a model of a disk load with a radius of 20° centered on the Thaumasia plateau. They determined a range of 3 – 51 km for the elastic thickness and a range of 2.71 – 3.31 g/cm^3 for the load density. Since the fit is done in the spatial domain on the line-of-sight acceleration with $\ell \geq 5$, long wavelengths dominate the signal with angular wavelengths of 20°–40°, that is $\ell \approx 9$ –18 (the disk model also has a very large spatial scale). The

analysis of *Williams et al.* [2008] thus corresponds to a much larger window than the one used in our analysis, without including acceleration perturbations at short wavelengths. We could do a 2D analysis with a large window (say of angular radius 30°) but the correlation would be rather low, between 0.6 and 0.9. The 2D admittance analysis of the region called Thaumasia in *Williams et al.* [2008] is dominated by Valles Marineris and will be discussed in section 5.5. *Dohm et al.* [2009] undertook another analysis of the gravity signal on a 1D profile across the Claritas rise (along a parallel defined by 28.5°S and 255°E – 262°E), using a simple top loading model ($\rho_t = \rho_c$). They found good fits either with a low density (2.3 – 2.75 g/cm 3) and an elastic thickness in the range 31 – 61 km, or with a high density (3.15 – 3.25 g/cm 3) and a much smaller elastic thickness (9 – 14 km). As in *Williams et al.* [2008], the gravity signal is analyzed in the spatial domain (short wavelengths are discarded) so that a comparison with our results is not justified.

[89] Small load densities are not compatible with the basaltic composition of the lava flows in the Tharsis province as discussed in section 5.3. *Dohm et al.* [2009] however showed with TES data that the mineralogy of the Claritas rise is better understood as felsic (granite/granodiorite) than basaltic, so that the density could be significantly smaller than the density of basaltic lava flows (on Earth, granite has a density of about 2.65 g/cm 3). Porosity due to impacts [*Clifford*, 1993] or to hydrothermal alteration followed by the formation of interstitial ice [*McGovern et al.*, 2002] can lower the density of the original rock. For example, *Nimmo* [2002] modeled the crust in the dichotomy area south of Elysium as being made of top layer of regolith with low density underlain by a higher density crust. Following *Clifford* [1993], we assume that the porosity decays exponentially with depth (decay constant of 2.82 km) and that the surface porosity is either $\Phi = 20\%$ (as on the Moon) or $\Phi = 50\%$ (as in the Martian soil analyzed by the Viking landers). If the pore-free density is 2.65 g/cm 3 , the average density in the top 4 km is 2.4 g/cm 3 ($\Phi = 20\%$) or 1.9 g/cm 3 ($\Phi = 50\%$) if the pores are empty, and 2.5 g/cm 3 ($\Phi = 20\%$) or 2.2 g/cm 3 ($\Phi = 50\%$) if the pores are filled with ice. The slightly different porosity decay law considered by *Wilson and Head* [1994] gives similar results. Alternatively, low densities can be explained by a sedimental origin of the rocks but there is as yet no other evidence supporting this hypothesis. In any case, low densities cannot be excluded in the Thaumasia highlands.

[90] Nevertheless, top loading models with a small density exclude very small values for the elastic thickness, which seems difficult to reconcile with the direct estimates of *Grott et al.* [2005, 2007] as well as with the small elastic thickness predicted by *Grott and Breuer* [2010] for features formed during the Noachian [*Dohm and Tanaka*, 1999; *Dohm et al.*, 2001]. Magnetic anomalies at Claritas also point to a Noachian age because magmatic intrusions must have stopped in this area before the cessation of the dynamo [*Johnson and Phillips*, 2005]. If we require that the surface density is not small and that the elastic thickness is small, the presence of bottom loading becomes unavoidable in the Thaumasia highlands, especially at Claritas. Another argument in favor of bottom loading is that it fits much better the admittance at

high harmonic degrees at Claritas. Bottom loading at Claritas rise could signal the presence of a volcanic plume at the time of the formation of the highlands [*Dohm et al.*, 2009]. Good fits with bottom loading at the Moho require that the crust density is high (resp. low) at Claritas (resp. Coracis), meaning that the bottom load has a large (resp. small) vertical extension at Claritas (resp. Coracis) because of the small (resp. large) density contrast with the mantle.

5.5. Valles Marineris

[91] Let us first consider Valles Marineris in its entirety. As observed by *McGovern et al.* [2002, 2004b], modeling Valles Marineris depends very much on assumptions about bottom loading. Short-wavelength ($\ell > 50$) MEX MaRS data yield rather low densities (2.5 – 2.7 g/cm 3) if there is no bottom loading, and significantly higher densities (2.7 – 3.1 g/cm 3) if bottom loading is present. Short-wavelength data cannot decide between the two options, but the spectral average at longer wavelength ($\ell > 30$) of profiles in the Middle West section can only be explained if significant bottom loading is present. These results are confirmed by the 2D analysis of Valles Marineris gravity (VM-Global) with top/bottom models (Figure 16 and Table 7). That top loading models require a low surface density at Valles Marineris was already found by *McKenzie et al.* [2002], who made a 2D admittance analysis of MGS line-of-sight profiles in the region (35°S to 25°N , 260°E to 350°E), obtaining a best fit with a density of 2.35 g/cm 3 and an elastic thickness of 53 km.

[92] A more diverse picture is revealed when examining parts of Valles Marineris. For the purpose of 2D spatio-spectral analysis, we divided the valley into four sections in which the coherence between gravity and topography is high (see Figure 5 and Table 2). The Far East section extends beyond the troughs to include outflow channels and chaotic terrain [*Lucchitta et al.*, 1992]. The admittance curves for the four sections look very different (Figure 12), suggesting that a unified model (i.e. with the same parameter values for all sections) will run into problems. We could not find any model giving a good fit at VM-Far West. Top/bottom models give acceptable fits at the other sections. Bottom loading (of positive type) is required at VM-Middle West but not at VM-Middle East; it only slightly improves the fit at VM-Far East (one should take care of rejecting models in which the local crust thickness is negative, see section 3.2.2). If bottom loading is absent, load densities are small (2.20 – 2.45 g/cm 3 , see Figure 16). As noted above, bottom loading shifts the possible loading densities to higher values and extends their admissible ranges, so that we cannot constrain with confidence the load density at VM-Middle West. Low densities are compatible with remote sensing observations only if sedimentary layers are dominant in the canyon walls, which does not seem to be the case (see section 5.1).

[93] Top/bottom models favor large values of the elastic thickness: $T_e > 80$, 110 and 120 km at VM-Middle West, Middle East and Far East, respectively (Model TB2, see Table 7). The results of top/bottom models are compatible with the lower resolution study of *McGovern et al.* [2002, 2004b], who found either low densities (2.1 – 2.5 g/cm 3) in the absence of bottom loading, or higher densities (2.9 g/cm 3) in the presence of bottom loading, with a large elastic

thickness in both cases. Analyzing three targets (Hebes, eastern Candor Chasma and Capri Chasmata), *McGovern et al.* [2002, 2004b] estimated that the required amount of bottom loading decreased from west to east and interpreted it as the signal of dike intensity decreasing when moving away from the supposed magma source in central Tharsis. This interpretation is compatible with the required bottom loading at VM-Middle West, that is to the west of the topographic step marked by the Coprates Rise. This change in bottom loading coincides with the composition boundary proposed by *Flahaut et al.* [2012]. Whatever the amount of bottom loading, the estimated elastic thickness is much larger than the 30 km value predicted by thermal models [*Grott and Breuer, 2010*] during the Hesperian. Note that *McGovern et al.* [2002, 2004b] dated Valles Marineris to the Hesperian-Amazonian epoch, but stratigraphic and structural analysis indicate that the major episode of trough development occurred from Early to Late Hesperian, with erosion continuing until the Late Amazonian [*Witbeck et al., 1991; Lucchitta et al., 1992; Carr and Head, 2010*]. Confirming this dating, crater counting by *Quantin et al.* [2004] showed that the floors of Coprates and Ganges Chasmata are up to 3.5 Ga old (Early Hesperian) while landslides occurred until 50 Ma ago. How can the elastic thickness be so large if the valley system formed during the Early Hesperian?

[94] As an alternative, we tried the scenario of *Andrews-Hanna* [2011], in which Valles Marineris troughs form in isostatic equilibrium with sedimentary filling later removed by erosion, leaving behind the so-called interior layered deposits [e.g., *Murchie et al., 2009*]. We modeled this two-stage process with two densities (ρ_{r1} for the cliff rocks and ρ_{r2} for the sediments) and two elastic thicknesses (T_{e1} for the formation of the troughs and T_{e2} for the later flexural uplift). Our top/top models give better fits than top/bottom models in all sections (comparing models with the same number of free parameters), especially when including low degrees associated with the Tharsis rise. However some problems remain: (1) only long wavelengths ($\ell < 40$, that is $\lambda \gtrsim 500$ km) can be fitted at VM-Far West, (2) the fit could be better at VM-Middle East and Far East (see Figure 12). T_{e1} must be small at VM-Middle West but is weakly constrained elsewhere, whereas T_{e2} must be larger than 100 km everywhere, implying that the later flexural uplift was small. If the canyon floor was initially at the surface before subsidence and sedimentary infilling [*Andrews-Hanna, 2011*], the small elastic thickness during the first stage is compatible with the Hesperian age of trough formation. By contrast, the larger elastic thickness during the removal of sediments is consistent with a Late Amazonian age [*Grott and Breuer, 2010*]. Finally, the density of the cliff rocks is favored to be low (best fits at 2.15–2.40 g/cm³ in the three sections fitted with Model TT1a). The density of the sediments cannot be constrained. In the scenario of *Andrews-Hanna* [2011], troughs are initiated by the collapse of blocks between parallel dikes. The inclusion of bottom loading thus seems a necessary ingredient of the model and could potentially solve the problem of too low densities. In conclusion, models based on a multistage formation process of Valles Marineris look promising but are probably too simple yet, at least in the version adopted in this paper, to adequately reproduce the relation between gravity and

topography. Unfortunately, gravity data cannot be used to determine whether Valles Marineris was once filled with low-density sediments.

6. Conclusions

[95] Using the most recent Martian gravity data provided by low altitude spacecraft (pericenter altitudes between 255 km and 330 km), we studied the surface density and the lithospheric structure in the Tharsis province. At very large scale, the Tharsis bulge stands as a geological feature in its own right, but at smaller scale it appears to be populated by very diverse structures with complex histories and extreme contrasts in size. For example, the volume of the largest volcano (Olympus Mons) is equivalent to the combined volume of the Tharsis Montes [*Plescia, 2004*] and the total volume of these four volcanoes would not fill Valles Marineris to the rim. All other structures are dwarfed in size relative to the large volcanoes and Valles Marineris. In order to exploit the gravity and topography data to its full resolution, we must take care to study each feature in isolation, otherwise the signal can be distorted by the contributions of other geological features. With lithospheric flexure models in mind, we investigated all targets (within Tharsis province) where the correlation between gravity and topography is high: the large shield volcanoes in the northwest (plus Elysium Mons for completeness), the Thaumasia highlands in the southeast and Valles Marineris in the east.

[96] At the large volcanoes, the density of the topography is high (3.0–3.4 g/cm³) in agreement with the density of Martian meteorites. Buoyant bottom loading is not present in significant amount, except maybe at Olympus Mons where its large vertical extension under the Moho could signal the presence of a mantle plume at the time of loading. Top/bottom models are not appropriate at Pavonis and Alba Montes while they require extreme values for the crust parameters at Olympus and Ascraeus Montes. Top/top models suggest that: (1) the volcanic shields themselves are of high density, not the surrounding topography, (2) all volcanoes have deep narrow roots of high density, except Olympus Mons where the root is shallow, (3) the elastic thickness of the lithosphere is large at Olympus Mons and is small at the other volcanoes. These results can be interpreted in two ways. In the first scenario, the construction of large volcanoes (except Ascraeus) began with andesitic lava of lower density which was then buried under basaltic lava of higher density forming the main shield. The elastic thickness remained small throughout the process except at Olympus Mons where it was always large. Since the main edifices of Olympus Mons and the Tharsis Montes all formed during the early Hesperian, this picture suggests there were large spatial variations in the elastic thickness at that time. The formation of the three Tharsis Montes began with Arsia Mons, followed by Pavonis Mons and finally by Ascraeus Mons. At Ascraeus Mons, the density of the extruded lava decreased at a later stage, so that the top of the volcano is of lower density. In the second scenario, all volcanoes formed on a very rigid lithosphere which also supported the supplementary load of high-density magma chambers and more generally igneous intrusions under the volcanoes. This scenario does not require large spatial variations of the elastic thickness, but implies either that the elastic thickness was already large

during the Hesperian or that the main building phase occurred later in the Amazonian.

[97] In the Thaumasia highlands, models without bottom loading can explain the gravity signal but require small load densities and a large elastic thickness. It is possible that the surface density is small, depending on the rock mineralogy and porosity. However a large elastic thickness conflicts with the Noachian age of the features and with estimates of the elastic thickness from fault modeling. The presence of bottom loading thus seems likely: the elastic thickness can be smaller and the load density higher. Bottom loading at the time of formation of the Thaumasia highlands could be explained by the presence of a plume which must have become extinct before the end of the global magnetic dynamo.

[98] Because of its extraordinary length, we divided Valles Marineris into four sections. The westernmost section cannot be fitted with any of our models. Top/bottom models require bottom loading in the Middle West section but not in the two eastern sections, in agreement with the hypothesis of dike intensity decreasing with distance from central Tharsis [McGovern *et al.*, 2002]. These models predict a large elastic thickness incompatible with the Hesperian age of the canyon. An interesting alternative is provided by a particular version of top/top models, in which the trough is formed with sedimentary infilling before being emptied of it by erosion [Andrews-Hanna, 2011]. The elastic thickness in the first phase of trough formation may have been small as expected from the Hesperian age of the canyon floor, whereas the elastic thickness at the time of sedimentary erosion was very large (compatible with an Amazonian age). A better mechanical model for Valles Marineris probably requires the combination of a multistage process (with at least two elastic thicknesses) with bottom loading caused by dense mafic dikes, as the ones recently identified by Flahaut *et al.* [2011] in the lower walls of Coprates Chasma. Another argument in favor of bottom loading is that it shifts the possible range of wall rock densities to higher values, otherwise the most likely density is small.

[99] Contrary to expectations, the increase in the resolution of the gravity field has not led to a better constraint on the elastic thickness. One reason is the decreasing sensitivity of the gravity signal on the elastic thickness as the wavelength gets shorter. Another reason is the existence of trade-offs with other unknown parameters such as the crust density, crust thickness and the amount of bottom loading. Existing maps of the crust thickness depend on unverified assumptions about the crust density; this situation is not going to improve as long as seismic experiments are not set up [Lognonné and Johnson, 2007]. By contrast, the load density should be better determined as the resolution increases. The resolution is however not yet high enough to allow us to decrease the window size up to the point where the surface (or load) density is uniform within the window. We indeed showed that models with spatial variations of density, such as the top/top models developed in this paper, fit better the data than bottom loading models without increasing the number of parameters. Smaller windows, however, do not solve the problem of determining vertical density variations. Besides, it is questionable to localize gravity with a window smaller than the target size (for example a volcano) because of boundary effects caused by windowing. In any case the accumulation of gravity data is a slow process (the resolution

increased by 50% from MGS to MRO) so that smaller windows are not the priority.

[100] Lithospheric models used in admittance analysis can still be improved on the basis of geological arguments. Spatially varying densities and elastic thicknesses evolving with time are two ingredients tried in this paper but other possibilities exist. The point is not to multiply the number of parameters, but rather to find which ones are the most relevant. The comparison of three different generic flexure models (TB0, TB0* and TT0) suggests that the free crustal parameters (thickness and density) should be dropped in favor of free bottom load parameters. These new parameters could be the lateral extension of the bottom load and its density contrast with the crust or mantle. We also observed that the relation between gravity and topography is not isotropic. Instead of ignoring this information, further modeling with varying densities could use the directional dependence of the admittance (or gain factor) as a constraint on the models.

Appendix A: Simple Flexure Model

[101] We give here a simplified version of the top/bottom model with bottom loading at the Moho (see section 3.2.2). We work in the mass-sheet approximation, neglect the effect of the geoid and consider the gravity anomaly prior to localization. With these assumptions, the spherical harmonic components of the gravity anomaly and topography are linearly related:

$$g_{\ell m} = 4\pi G \rho_t \left(\frac{\ell + 1}{2\ell + 1} \right) (1 - K(\ell)) h_{\ell m}, \quad (\text{A1})$$

where (ℓ, m) denote the harmonic degree and order and ρ_t is the loading density. The *depth-filtered degree of compensation* $K(\ell)$ represents the sum of the contributions of the interior density anomalies.

[102] Before defining $K(\ell)$, we need to define the degree of compensation for top (resp. bottom) loading only [Turcotte *et al.*, 1981]:

$$C_x(\ell) = \frac{\lambda_3(\ell)}{\sigma_x \lambda_1(\ell) + \tau_x \lambda_2(\ell) + \lambda_3(\ell)} \quad (x = t \text{ or } b). \quad (\text{A2})$$

$C_x(\ell)$ varies between 0 (no compensation; infinitely rigid lithosphere) and 1 (full compensation or Airy isostasy, always achieved for $\ell = 1$). The dimensionless functions $\lambda_i(\ell)$ read

$$\begin{aligned} \lambda_1(\ell) &= \ell(\ell + 1)(\ell(\ell + 1) - 2)^2, \\ \lambda_2(\ell) &= \ell(\ell + 1) - 2, \\ \lambda_3(\ell) &= \ell(\ell + 1) - 1 + \nu. \end{aligned} \quad (\text{A3})$$

Equations (A2)–(A3) correspond to those of Turcotte *et al.* [1981] and McGovern *et al.* [2002] with a correction due to a missing term in the flexure equation [Willemann and Turcotte, 1982], so that $f_1(\ell)$ should be replaced by $\lambda_1(\ell)$ in equations A5 and A11 of McGovern *et al.* [2002]. Our degrees of compensation are related to the transfer functions

of McGovern *et al.* [2002] by $C_t = -\alpha^t(\rho_m - \rho_t)/\rho_t$ and $C_b = -(\rho_m - \rho_b)/(\rho_b(1 + \alpha^b))$, with densities defined below.

[103] The dimensionless parameters τ_x and σ_x ($x = t$ or b) for membrane flexure and bending read

$$\tau_x = \frac{ET_e}{R^2g(\rho_m - \rho_x)}, \quad (\text{A4})$$

$$\sigma_x = \frac{\tau_x}{12(1 - \nu^2)} \left(\frac{T_e}{R} \right)^2. \quad (\text{A5})$$

E is Young's modulus, ν is Poisson's ratio, T_e is the elastic thickness and g is the surface gravity. The densities of the top load, crust, mantle and bottom load are respectively denoted by ρ_t , ρ_c , ρ_m and ρ_b , while $\rho_b = \rho_m - \rho_B$ is the bottom density anomaly.

[104] If there is no bottom loading, $K(\ell)$ is given by

$$K(\ell) = \left(\frac{\rho_c - \rho_t}{\rho_m - \rho_t} + \frac{\rho_m - \rho_c}{\rho_m - \rho_t} \left(1 - \frac{T_c}{R} \right)^{\ell+2} \right) C_t(\ell), \quad (\text{A6})$$

where T_c is the crust thickness. The first term represents the contribution of the crust/load interface and the second term results from the deflection of the Moho. Note that equations (A1) and (A6) are equivalent to equations A.4–A.5 of Wieczorek [2008] because of the identity

$$C_t(\ell) = \frac{(\rho_m - \rho_t)C_l^0}{\rho_m - \rho_t C_l^0}. \quad (\text{A7})$$

[105] If bottom loading occurs at the Moho in phase with the top load and if $\rho_B = \rho_t = \rho_c$, $K(\ell)$ is given by

$$K(\ell) = \left(1 - \frac{T_c}{R} \right)^{\ell+2} \frac{C_t(\ell) + \tilde{f}(\ell)/C_b(\ell)}{1 + \tilde{f}(\ell)}, \quad (\text{A8})$$

where the function $\tilde{f}(\ell)$ is the ratio (at degree ℓ) of the topography resulting from bottom loading to the topography resulting from top loading. For arbitrary ρ_t and ρ_B , $\tilde{f}(\ell)$ is related to the bottom loading ratio f (ratio of bottom load weight to top load weight before deflection) by

$$\tilde{f}(\ell) = \frac{\rho_t}{\rho_m - \rho_t} C_t(\ell) f. \quad (\text{A9})$$

Bottom loading of positive type corresponds to $f > 0$. In the limit $f = 1$, the top load is completely supported by the bottom load (isostasy) so that the degree of compensation becomes independent of the elastic thickness: $K(\ell) = (1 - T_c/R)^{\ell+2}$.

[106] If bottom loading is of negative type ($f < 0$) with $f \leq -(\rho_m - \rho_t)/\rho_t$, a positive real number x exists such that $\tilde{f}(x) = -1$. In that case, $K(\ell)$ can be nearly singular at the harmonic degree ℓ closest to x : top and negative-type bottom loading combine to give near-zero topography at some degree ℓ .

Appendix B: Influence of Parameters

[107] Estimating model parameters can only be successful if the parameters have large effects that are very different

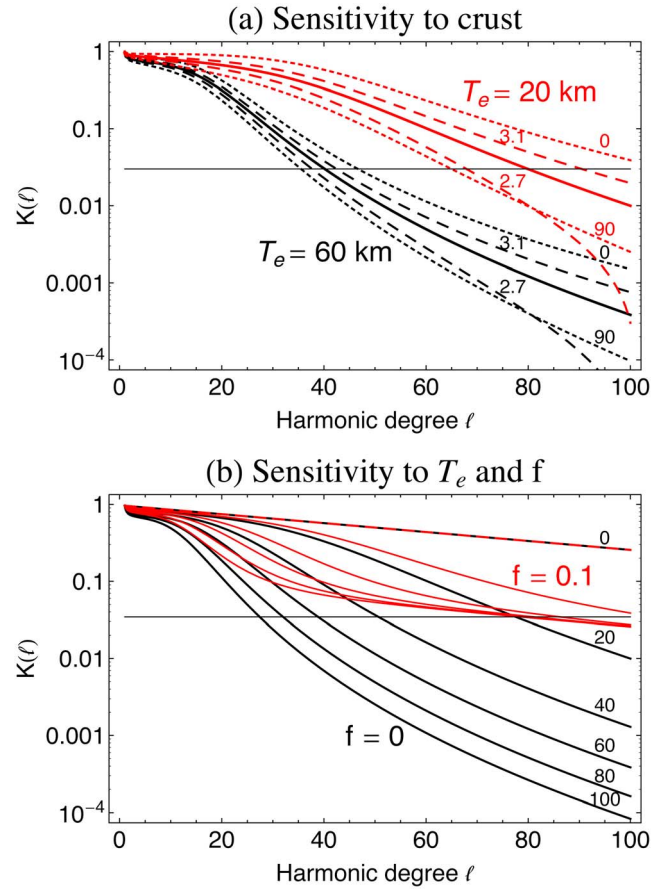


Figure B1. Depth-filtered degree of compensation $K(\ell)$ vs harmonic degree. (a) Influence of crust thickness T_c and crust density ρ_c . Reference curves are drawn as solid curves: $T_c = 45$ km, $\rho_c = \rho_t = 2.9$ g/cm³, and $T_e = 60$ km (black) or $T_e = 20$ km (red). Dotted curves differ from the reference curves by $T_c = 0$ or 90 km (see labels). Dashed curves differ from the reference curves by $\rho_c = 2.7$ or 3.1 g/cm³ (see labels). (b) Influence of elastic thickness T_e and bottom loading ratio f ($T_c = 45$ km, $\rho_c = 2.9$ g/cm³). Black curves are for top loading only ($f = 0$) and are labeled by T_e (in km). Red curves are for bottom loading with $f = 0.1$ and are similarly ordered from top to bottom (the curve for $T_e = 0$ km is identical with the top curve without bottom loading). The horizontal line indicates the threshold above which the compensation cannot be neglected if the density needs to be determined at a precision of 0.1 g/cm³. In all cases $\rho_m = 3.5$ g/cm³, $E = 100$ GPa, $\nu = 0.25$.

from each other. It is thus interesting to see which parameters have the most effect on the results. We use here the simplified equations of Appendix A.

[108] Suppose first that there is no bottom loading but that the load density ρ_t differs from the crust density ρ_c . Figure B1a shows that the crust thickness and density have a rather weak influence on the gravity anomaly through the depth-filtered degree of compensation, especially beyond $\ell = 50$. Since ρ_t appears as a global multiplying factor in equation (A1), gravity anomalies are very sensitive to the value of ρ_t .

[109] Suppose now that there is bottom loading at the Moho but that the densities of the top and bottom loads are equal to the crust density. Figure B1b shows that the elastic thickness T_e and the bottom loading ratio f have a strong effect on the gravity anomaly through $K(\ell)$. If we want to determine the surface density at a precision of 0.1 g/cm^3 without fitting the elastic thickness, $K(\ell)$ should be smaller than $0.1/2.9$, which for example occurs at degree $\ell = 50$ for an elastic thickness larger than 40 km if $f = 0$. However this is not true anymore when bottom loading is present, even in small amounts (here $f = 0.1$). As a caveat, we note that in-phase bottom loading is not a reasonable hypothesis at very short wavelengths.

[110] Flexure models also depend on parameters that are kept fixed: mantle density, Young's modulus and Poisson's ratio. Different interior models predict similar values of the subcrustal mantle density: $3.4\text{--}3.55 \text{ g/cm}^3$ [Rivoldini et al., 2011, Figure 17]. In fact, what matters are the density contrasts between the mantle, crust and load. Uncertainties of the mantle density are thus absorbed in the crust and load densities. As membrane effects are negligible at short wavelength (see equations (A4)), Young's modulus only appears in the combination ET_e^3 (see equation (A5)), so that a 30% variation in E results in a 10% variation in T_e . Poisson's ratio can be neglected in $\lambda_3(\ell)$ when ℓ is large (see equation (A3)) so that it only appears in the combination $1 - \nu^2$ (see equations (A5)). The variation of ν around its fixed value of 0.25 has thus a very small impact on T_e estimates.

[111] In conclusion, it is difficult to determine the thickness and density of the crust with admittance analysis which is more sensitive to the loading density, the elastic thickness and the bottom loading ratio.

Appendix C: Statistics

[112] A fitting procedure should provide (i) parameters, (ii) error estimates on the parameters, and (iii) a statistical measure of goodness-of-fit [Press et al., 1992, chap. 15]. Belleguic et al. [2005] and Williams et al. [2008] interpret the total misfit nM^2 (see equation (10)) as a chi-square statistic with which one can compute confidence intervals for the model parameters [Press et al., 1992]. This interpretation would be true if the admittances $Z^{obs}(i)$ were independent random variables with normal distributions. The estimates of the admittance at different frequencies are however correlated by data tapering. For example, the 2D cross-spectral estimate at a given degree ℓ depends on the global spectrum over the range $|\ell - L| \leq \ell \leq |\ell + L|$ [Wieczorek and Simons, 2005], where L is the bandwidth of the window. A similar effect appears in the 1D case. Therefore the chi-square statistic must take into account correlations between variables [Tarantola, 2005]:

$$\chi^2 = (\mathbf{Z}^{obs} - \mathbf{Z}^{pred})^t \mathbf{C}^{-1} (\mathbf{Z}^{obs} - \mathbf{Z}^{pred}), \quad (\text{C1})$$

where \mathbf{C} is the covariance matrix associated with the random vector $\mathbf{Z}^{obs} - \mathbf{Z}^{pred}$. If the components of the random vector are uncorrelated, the covariance matrix is diagonal so that the chi-square is related to the RMS misfit by $\chi^2 = nM^2$.

[113] Before discussing covariance estimates, we note that Belleguic et al. [2005] compute the posterior probability distribution for model parameters by attributing to each model a probability $P \sim \exp(-M^2/2)$, in which M is the RMS misfit defined by equation (10). The origin of this formula is unclear: it is equivalent to the probability of n independent variables with errors multiplied by \sqrt{n} . In Bayesian inversion theory, the posterior probability of a specific model depends on the chi-square function [Tarantola, 2005]:

$$P \sim \exp(-\chi^2/2), \quad (\text{C2})$$

where χ^2 is defined by equation (C1) (assuming that we have no a priori information on the model parameters). Thus this approach also requires the knowledge of the covariance matrix.

[114] The difficulty lies in estimating the covariance matrix, either from data or from theoretical arguments. In multitaper analysis, spectral estimates associated with orthogonal tapers are approximately uncorrelated in the 1D case [Percival and Walden, 1993] as well as in the 2D spherical case [Wieczorek and Simons, 2005, 2007]. In the 1D case, the covariance matrix can thus be estimated by the jackknife covariance [Thomson and Chave, 1991]. However, the resulting covariance matrix is singular because its rank is at most equal to the number of frequency bands, which is in our case less than the number of frequency bands. Though we can decide to reduce the number of frequency bands, the covariance matrix remains ill-conditioned because of the small sample size. Another possibility consists in regularizing the covariance matrix by shrinking off-diagonal elements [Schäfer and Strimmer, 2005] but the application of this method to the 1D pericenter passes resulted in a nearly diagonal covariance matrix which is unrealistic.

[115] In the 2D spherical case, the covariance cannot be estimated with the method just described because only one taper is available. Even with several tapers, it would be problematic to compute the covariance of spectral estimates at different degrees, as the number of samples varies with the degree (the sum on the harmonic order m gives $2\ell + 1$ independent estimates at each degree ℓ , see equation (5)). Assuming that the global fields are generated by stationary stochastic processes, Wieczorek and Simons [2007] derived a formula for the covariance of cross-spectral estimates at different degrees and orders (see also Dahlen and Simons [2008] for a detailed discussion of the covariance of spherical spectral estimates). Since the Tharsis rise with its large volcanoes and Valles Marineris are both incompatible with the assumption of global uniformity, we do not think that this formula yields a correct estimate of the covariance (besides such a covariance matrix would probably be ill-conditioned). We will thus not give a statistical interpretation because of our insufficient knowledge of the correlations between localized admittances.

[116] **Acknowledgments.** M. Beuthe, S. Le Maistre and P. Rosenblatt are financially supported by the European Space Agency in collaboration with the Belgian Federal Science Policy Office. M. Pätzold acknowledges support from Deutsches Zentrum für Luft- und Raumfahrt, Bonn, under grant 50QM1004. The authors thank the MEX Science Operations Team for the proper scheduling of the gravity passes and all the people involved in the MEX mission at ESTEC, ESOC, ESAC, JPL and the ESA and DSN ground station complexes for their continuous support. In particular, we thank the

MEX Project Scientists Olivier Witasse and Agustin Chicarro. We also thank Richard Simpson for the transfer of the DSN data. The paper greatly benefited from thorough reviews by Matthias Grott and two anonymous reviewers.

References

- Andrews-Hanna, J. C. (2011), The formation of Valles Marineris, Mars, *Lunar Planet. Sci., XLII*, Abstract 2182.
- Audet, P., and J.-C. Mareschal (2007), Wavelet analysis of the coherence between Bouguer gravity and topography: Application to the elastic thickness anisotropy in the Canadian Shield, *Geophys. J. Int.*, **168**, 287–298, doi:10.1111/j.1365-246X.2006.03231.x.
- Audet, P., A. M. Jellinek, and H. Uno (2007), Mechanical controls on the deformation of continents at convergent margins, *Earth Planet. Sci. Lett.*, **264**, 151–166, doi:10.1016/j.epsl.2007.09.024.
- Belleguic, V., P. Lognonné, and M. Wicczorek (2005), Constraints on the Martian lithosphere from gravity and topography data, *J. Geophys. Res.*, **110**, E11005, doi:10.1029/2005JE002437.
- Bendat, J. S., and A. G. Piersol (2000), *Random Data: Analysis and Measurement Procedures*, John Wiley, New York.
- Beuthe, M., P. Rosenblatt, V. Dehant, J.-P. Barriot, M. Pätzold, B. Häusler, Ö. Karatekin, S. Le Maistre, and T. Van Hoolst (2006), Assessment of the Martian gravity field at short wavelength with Mars Express, *Geophys. Res. Lett.*, **33**, L03203, doi:10.1029/2005GL024317.
- Beverington, P. R., and D. K. Robinson (2003), *Data Reduction and Error Analysis*, 3rd ed., McGrawHill, Boston.
- Beyer, R. A., and A. S. McEwen (2005), Layering stratigraphy of eastern Coprates and northern Capri Chasmata, Mars, *Icarus*, **179**, 1–23, doi:10.1016/j.icarus.2005.06.014.
- Bills, B. G., and F. G. Lemoine (1995), Gravitational and topographic isotropy of the Earth, Moon, Mars, and Venus, *J. Geophys. Res.*, **100**, 26,275–26,296, doi:10.1029/95JE02982.
- Bleacher, J. E., R. Greeley, D. A. Williams, S. R. Cave, and G. Neukum (2007), Trends in effusive style at the Tharsis Montes, Mars, and implications for the development of the Tharsis province, *J. Geophys. Res.*, **112**, E09005, doi:10.1029/2006JE002873.
- Boynton, W. V., et al. (2007), Concentration of H, Si, Cl, K, Fe, and Th in the low- and mid-latitude regions of Mars, *J. Geophys. Res.*, **112**, E12S99, doi:10.1029/2007JE002887.
- Carr, M. H., and J. W. Head (2010), Geologic history of Mars, *Earth Planet. Sci. Lett.*, **294**, 185–203, doi:10.1016/j.epsl.2009.06.042.
- Carter, L. M., B. A. Campbell, J. W. Holt, R. J. Phillips, N. E. Putzig, S. Mattei, R. Seu, C. H. Okubo, and A. F. Egan (2009), Dielectric properties of lava flows west of Ascraeus Mons, Mars, *Geophys. Res. Lett.*, **36**, L23204, doi:10.1029/2009GL041234.
- Christensen, P. R., et al. (2003), Morphology and composition of the surface of Mars: Mars Odyssey THEMIS results, *Science*, **300**, 2056–2061, doi:10.1126/science.1080885.
- Clifford, S. M. (1993), A model for the hydrologic and climatic behavior of water on Mars, *J. Geophys. Res.*, **98**, 10,973–11,016, doi:10.1029/93JE00225.
- Comer, R. P., S. C. Solomon, and J. W. Head (1985), Mars: Thickness of the lithosphere from the tectonic response to volcanic loads, *Rev. Geophys.*, **23**, 61–92, doi:10.1029/RG023i001p00061.
- Dahlen, F. A., and F. J. Simons (2008), Spectral estimation on a sphere in geophysics and cosmology, *Geophys. J. Int.*, **174**, 774–807, doi:10.1111/j.1365-246X.2008.03854.x.
- Davis, D. J., and J. C. Andrews-Hanna (2011), Flexural response to sediment erosion and unloading at Valles Marineris, *Lunar Planet. Sci., XLII*, Abstract 2557.
- Dohm, J. M., and K. L. Tanaka (1999), Geology of the Thaumasia region, Mars: Plateau development, valley origins, and magmatic evolution, *Planet. Space Sci.*, **47**, 411–431, doi:10.1016/S0032-0633(98)00141-X.
- Dohm, J. M., K. L. Tanaka, and T. M. Hare (2001), Geologic map of the Thaumasia region of Mars, *U.S. Geol. Surv. Misc. Invest. Ser. Map*, **I-2650**.
- Dohm, J. M., et al. (2009), Claritas rise, Mars: pre-Tharsis magmatism?, *J. Volcanol. Geotherm. Res.*, **185**, 139–156, doi:10.1016/j.jvolgeores.2009.03.012.
- Edwards, C. S., P. R. Christensen, and V. E. Hamilton (2008), Evidence for extensive olivine-rich basalt bedrock outcrops in Ganges and Eos chasmata, Mars, *J. Geophys. Res.*, **113**, E11003, doi:10.1029/2008JE003091.
- El Maary, M. R., O. Gasnault, M. J. Toplis, D. Baratoux, J. M. Dohm, H. E. Newsom, W. V. Boynton, and S. Karunatillake (2009), Gamma-ray constraints on the chemical composition of the Martian surface in the Tharsis region: A signature of partial melting of the mantle?, *J. Volcanol. Geotherm. Res.*, **185**, 116–122, doi:10.1016/j.jvolgeores.2008.11.027.
- Flahaut, J., J. F. Mustard, C. Quantin, H. Clenet, P. Allemand, and P. Thomas (2011), Dikes of distinct composition intruded into Noachian-aged crust exposed in the walls of Valles Marineris, *Geophys. Res. Lett.*, **38**, L15202, doi:10.1029/2011GL048109.
- Flahaut, J., C. Quantin, H. Clenet, P. Allemand, J. F. Mustard, and P. Thomas (2012), Pristine Noachian crust and key geologic transitions in the lower walls of Valles Marineris: insights into early igneous processes on Mars, *Icarus*, doi:10.1016/j.icarus.2011.12.027, in press.
- Forsyth, D. W. (1985), Subsurface loading and estimates of the flexural rigidity of continental lithosphere, *J. Geophys. Res.*, **90**, 12,623–12,632, doi:10.1029/JB090iB14p12623.
- Grott, M., and D. Breuer (2008), The evolution of the Martian elastic lithosphere and implications for crustal and mantle rheology, *Icarus*, **193**, 503–515, doi:10.1016/j.icarus.2007.08.015.
- Grott, M., and D. Breuer (2010), On the spatial variability of the Martian elastic lithosphere thickness: Evidence for mantle plumes?, *J. Geophys. Res.*, **115**, E03005, doi:10.1029/2009JE003456.
- Grott, M., and M. Wicczorek (2011), Tyrrhena Patera, Mars: Evidence for a solidified magma chamber?, Abstract EPSC-DPS2011-376, presented at Joint Meeting of the European Planetary Science Congress and Division for Planetary Sciences of the American Astronomical Society, Nantes, France, 2–7 October.
- Grott, M., E. Hauber, S. C. Werner, P. Kronberg, and G. Neukum (2005), High heat flux on ancient Mars: Evidence from rift flank uplift at Coracis Fossae, *Geophys. Res. Lett.*, **32**, L21201, doi:10.1029/2005GL023894.
- Grott, M., E. Hauber, S. C. Werner, P. Kronberg, and G. Neukum (2007), Mechanical modeling of thrust faults in the Thaumasia region, Mars, and implications for the Noachian heat flux, *Icarus*, **186**, 517–526, doi:10.1016/j.icarus.2006.10.001.
- Guest, A., and S. E. Smrekar (2007), New constraints on the thermal and volatile evolution of Mars, *Phys. Earth Planet. Int.*, **164**, 161–176, doi:10.1016/j.pepi.2007.06.010.
- Hamilton, V. E., P. R. Christensen, H. Y. McSweeney Jr., and J. L. Bandfield (2003), Searching for the source regions of Martian meteorites using MGS TES: Integrating Martian meteorites into the global distribution of igneous materials on Mars, *Meteorit. Planet. Sci.*, **38**, 871–885, doi:10.1111/j.1945-5100.2003.tb00284.x.
- Hartmann, W. K. (2005), Martian cratering 8: Isochron refinement and the chronology of Mars, *Icarus*, **174**, 294–320, doi:10.1016/j.icarus.2004.11.023.
- Hartmann, W. K., and G. Neukum (2001), Cratering Chronology and the Evolution of Mars, *Space Sci. Rev.*, **96**, 165–194, doi:10.1023/A:1011945222010.
- Hauber, E., P. Brož, F. Jagert, P. Jodłowski, and T. Platz (2011), Very recent and wide-spread basaltic volcanism on Mars, *Geophys. Res. Lett.*, **38**, L10201, doi:10.1029/2011GL047310.
- Hauck, S. A., and R. J. Phillips (2002), Thermal and crustal evolution of Mars, *J. Geophys. Res.*, **107**(E7), 5052, doi:10.1029/2001JE001801.
- Hiesinger, H., J. W. Head, and G. Neukum (2007), Young lava flows on the eastern flank of Ascraeus Mons: Rheological properties derived from High Resolution Stereo Camera (HRSC) images and Mars Orbiter Laser Altimeter (MOLA) data, *J. Geophys. Res.*, **112**, E05011, doi:10.1029/2006JE002717.
- Hiller, K. H., G. P. O. Neukum, P. Janle, J. E. Guest, and R. M. C. Lopes (1982), Mars: Stratigraphy and gravimetry of Olympus Mons and its aureole, *J. Geophys. Res.*, **87**, 9905–9915, doi:10.1029/JB087iB12p09905.
- Ivanov, M. A., and J. W. Head (2006), Alba Patera, Mars: Topography, structure, and evolution of a unique late Hesperian-early Amazonian shield volcano, *J. Geophys. Res.*, **111**, E09003, doi:10.1029/2005JE002469.
- Jellinek, A. M., C. L. Johnson, and G. Schubert (2008), Constraints on the elastic thickness, heat flow, and melt production at early Tharsis from topography and magnetic field observations, *J. Geophys. Res.*, **113**, E09004, doi:10.1029/2007JE003005.
- Johnson, C. L., and R. J. Phillips (2005), Evolution of the Tharsis region of Mars: insights from magnetic field observations, *Earth Planet. Sci. Lett.*, **230**, 241–254, doi:10.1016/j.epsl.2004.10.038.
- Jozwiak, L. M., J. Isherwood, and J. C. Andrews-Hanna (2011), The formation history of Olympus Mons from paleo-topography, *Lunar Planet. Sci., XLII*, Abstract 2202.
- Kaiser, J. F., and W. A. Reed (1977), Data smoothing using low-pass digital filters, *Rev. Sci. Instrum.*, **48**, 1447–1457, doi:10.1063/1.1134918.
- Kiefer, W. S. (2004), Gravity evidence for an extinct magma chamber beneath Syrtis Major, Mars: a look at the magmatic plumbing system, *Earth Planet. Sci. Lett.*, **222**, 349–361, doi:10.1016/j.epsl.2004.03.009.
- Kiefer, W. S., and Q. Li (2009), Mantle convection controls the observed lateral variations in lithospheric thickness on present-day Mars, *Geophys. Res. Lett.*, **36**, L18203, doi:10.1029/2009GL039827.
- Kiefer, W. S., and R. J. Lillis (2011), Geophysical observations of Hadriaca Patera and Tyrrhena Patera, Mars: Implications for magma chamber structure and for the end of the Martian magnetic dynamo, *Lunar Planet. Sci., XLII*, Abstract 1662.

- Kirby, J. F., and C. J. Swain (2006), Mapping the mechanical anisotropy of the lithosphere using a 2D wavelet coherence, and its application to Australia, *Phys. Earth Planet. Int.*, **158**, 122–138, doi:10.1016/j.pepi.2006.03.022.
- Konopliv, A. S., S. W. Asmar, W. M. Folkner, Ö. Karatekin, D. C. Nunes, S. E. Smrekar, C. F. Yoder, and M. T. Zuber (2011), Mars high resolution gravity fields from MRO, Mars seasonal gravity, and other dynamical parameters, *Icarus*, **211**, 401–428, doi:10.1016/j.icarus.2010.10.004.
- Lang, N. P., L. L. Tornabene, H. Y. McSween Jr., and P. R. Christensen (2009), Tharsis-sourced relatively dust-free lavas and their possible relationship to Martian meteorites, *J. Volcanol. Geotherm. Res.*, **185**, 103–115, doi:10.1016/j.jvolgeores.2008.12.014.
- Lawrence, K. P., and R. J. Phillips (2003), Gravity/topography admittance inversion on Venus using niching genetic algorithms, *Geophys. Res. Lett.*, **30**(19), 1994, doi:10.1029/2003GL017515.
- Lillis, R. J., J. Dufek, J. E. Bleacher, and M. Manga (2009), Demagnetization of crust by magmatic intrusion near the Arsia Mons volcano: Magnetic and thermal implications for the development of the Tharsis province, Mars, *J. Volcanol. Geotherm. Res.*, **185**, 123–138, doi:10.1016/j.jvolgeores.2008.12.007.
- Lognonné, P., and C. Johnson (2007), Planetary seismology, in *Treatise on Geophysics*, vol. 10, *Planets and Moons*, edited by T. Spohn, pp. 69–122, Cambridge Univ. Press, Cambridge, U. K., doi:10.1016/B978-0-444-52748-6.00154-1.
- Lowry, A. R., and S. Zhong (2003), Surface versus internal loading of the Tharsis rise, Mars, *J. Geophys. Res.*, **108**(E9), 5099, doi:10.1029/2003JE002111.
- Lucchitta, B. K., A. S. McEwen, G. D. Clow, P. E. Geissler, R. B. Singer, R. A. Schultz, and S. W. Squyres (1992), The canyon system on Mars, in *Mars*, edited by H. H. Kieffer et al., pp. 453–492, Univ. of Ariz. Press, Tucson.
- Lucchitta, B. K., N. K. Isbell, and A. Howington-Kraus (1994), Topography of Valles Marineris: Implications for erosional and structural history, *J. Geophys. Res.*, **99**, 3783–3798, doi:10.1029/93JE03095.
- Macke, R. J., D. T. Britt, and G. J. Consolmagno (2011), Density, porosity, and magnetic susceptibility of achondritic meteorites, *Meteorit. Planet. Sci.*, **46**, 311–326, doi:10.1111/j.1945-5100.2010.01155.x.
- Malin, M. C., and K. S. Edgett (2000), Sedimentary rocks of early Mars, *Science*, **290**, 1927–1937, doi:10.1126/science.290.5498.1927.
- McEwen, A. S., M. C. Malin, M. H. Carr, and W. K. Hartmann (1999), Voluminous volcanism on early Mars revealed in Valles Marineris, *Nature*, **397**, 584–586, doi:10.1038/17539.
- McGovern, P. J., S. C. Solomon, D. E. Smith, M. T. Zuber, M. Simons, M. A. Wieczorek, R. J. Phillips, G. A. Neumann, O. Aharonson, and J. W. Head (2002), Localized gravity/topography admittance and correlation spectra on Mars: Implications for regional and global evolution, *J. Geophys. Res.*, **107**(E12), 5136, doi:10.1029/2002JE001854.
- McGovern, P. J., J. R. Smith, J. K. Morgan, and M. H. Bulmer (2004a), Olympus Mons aureole deposits: New evidence for a flank failure origin, *J. Geophys. Res.*, **109**, E08008, doi:10.1029/2004JE002258.
- McGovern, P. J., S. C. Solomon, D. E. Smith, M. T. Zuber, M. Simons, M. A. Wieczorek, R. J. Phillips, G. A. Neumann, O. Aharonson, and J. W. Head (2004b), Correction to “Localized gravity/topography admittance and correlation spectra on Mars: Implications for regional and global evolution,” *J. Geophys. Res.*, **109**, E07007, doi:10.1029/2004JE002286.
- McKenzie, D., and D. Fairhead (1997), Estimates of the effective elastic thickness of the continental lithosphere from Bouguer and free air gravity anomalies, *J. Geophys. Res.*, **102**, 27,523–27,552, doi:10.1029/97JB02481.
- McKenzie, D., and F. Nimmo (1997), Elastic thickness estimates for Venus from line of sight accelerations, *Icarus*, **130**, 198–216, doi:10.1006/icar.1997.5770.
- McKenzie, D., D. N. Barnett, and D.-N. Yuan (2002), The relationship between Martian gravity and topography, *Earth Planet. Sci. Lett.*, **195**, 1–16, doi:10.1016/S0012-821X(01)00555-6.
- McSween, H. Y., Jr. (2002), Leonard Medal Address: The rocks of Mars, from far and near, *Meteorit. Planet. Sci.*, **37**, 7–25, doi:10.1111/j.1945-5100.2002.tb00793.x.
- McSween, H. Y., T. L. Grove, and M. B. Wyatt (2003), Constraints on the composition and petrogenesis of the Martian crust, *J. Geophys. Res.*, **108**(E12), 5135, doi:10.1029/2003JE002175.
- McSween, H. Y., G. J. Taylor, and M. B. Wyatt (2009), Elemental composition of the Martian crust, *Science*, **324**, 736–739, doi:10.1126/science.1165871.
- Murchie, S., et al. (2009), Evidence for the origin of layered deposits in Candor Chasma, Mars, from mineral composition and hydrologic modeling, *J. Geophys. Res.*, **114**, E00D05, doi:10.1029/2009JE003343.
- Neukum, G., et al. (2004), Recent and episodic volcanic and glacial activity on Mars revealed by the High Resolution Stereo Camera, *Nature*, **432**, 971–979, doi:10.1038/nature03231.
- Neukum, G., A. T. Basilevsky, T. Kneissl, M. G. Chapman, S. van Gasselt, G. Michael, R. Jaumann, H. Hoffmann, and J. K. Lanz (2010), The geologic evolution of Mars: Episodicity of resurfacing events and ages from cratering analysis of image data and correlation with radiometric ages of Martian meteorites, *Earth Planet. Sci. Lett.*, **294**, 204–222, doi:10.1016/j.epsl.2009.09.006.
- Neumann, G. A., M. T. Zuber, M. A. Wieczorek, P. J. McGovern, F. G. Lemoine, and D. E. Smith (2004), Crustal structure of Mars from gravity and topography, *J. Geophys. Res.*, **109**, E08002, doi:10.1029/2004JE002262.
- Neumann, G. A., F. G. Lemoine, D. E. Smith, and M. T. Zuber (2008), Marscrust3: A crustal thickness inversion from recent MRO gravity solutions, *Lunar Planet. Sci.*, **XXXIX**, Abstract 2167.
- Nimmo, F. (2002), Admittance estimates of mean crustal thickness and density at the Martian hemispheric dichotomy, *J. Geophys. Res.*, **107**(E11), 5117, doi:10.1029/2000JE001488.
- Nimmo, F., and K. Tanaka (2005), Early crustal evolution of Mars, *Annu. Rev. Earth Planet. Sci.*, **33**, 133–161, doi:10.1146/annurev.earth.33.092203.122637.
- Pätzold, M., et al. (2004), MaRS: Mars Express Orbiter Radio Science, *Eur. Space Agency Spec. Publ.*, **SP-1240**, 141–163.
- Pätzold, M., et al. (2009), MaRS: Mars Express Radio Science Experiment, *Eur. Space Agency Spec. Publ.*, **SP-1291**, 217–245.
- Pauer, M., and D. Breuer (2008), Constraints on the maximum crustal density from gravity topography modeling: Applications to the southern highlands of Mars, *Earth Planet. Sci. Lett.*, **276**, 253–261, doi:10.1016/j.epsl.2008.09.014.
- Percival, D. B., and A. T. Walden (1993), *Spectral Analysis for Physical Applications: Multitaper and Conventional Univariate Techniques*, Cambridge Univ. Press, New York.
- Phillips, R. J. (1994), Estimating lithospheric properties at Atla Regio, Venus, *Icarus*, **112**, 147–170, doi:10.1006/icar.1994.1175.
- Plescia, J. B. (2004), Morphometric properties of Martian volcanoes, *J. Geophys. Res.*, **109**, E03003, doi:10.1029/2002JE002031.
- Press, W. H., S. A. Teukolsky, W. T. Vetterling, and B. P. Flannery (1992), *Numerical Recipes in FORTRAN. The Art of Scientific Computing*, 2nd ed., Cambridge Univ. Press, New York.
- Quantin, C., P. Allemand, N. Mangold, and C. Delacourt (2004), Ages of Valles Marineris (Mars) landslides and implications for canyon history, *Icarus*, **172**, 555–572, doi:10.1016/j.icarus.2004.06.013.
- Rivoldini, A., T. van Hoolst, O. Verhoeven, A. Mocquet, and V. Dehant (2011), Geodesy constraints on the interior structure and composition of Mars, *Icarus*, **213**, 451–472, doi:10.1016/j.icarus.2011.03.024.
- Robbins, S. J., G. D. Achille, and B. M. Hynek (2011), The volcanic history of Mars: High-resolution crater-based studies of the calderas of 20 volcanoes, *Icarus*, **211**, 1179–1203, doi:10.1016/j.icarus.2010.11.012.
- Ross Taylor, S., and S. M. McLennan (2008), *Planetary Crusts: Their Composition, Origin and Evolution*, Cambridge Univ. Press, Cambridge, U. K.
- Ruiz, J., P. J. McGovern, A. Jiménez-Díaz, J.-P. López, V. Williams, B. C. Hahn, and R. Tejero (2011), The thermal evolution of Mars as constrained by the paleo-heat flows, *Icarus*, **215**, 508–517, doi:10.1016/j.icarus.2011.07.029.
- Schäfer, J., and K. Strimmer (2005), A shrinkage approach to large-scale covariance matrix estimation and implications for functional genomics, *Stat. App. Genet. Mol. Biol.*, **4**, 32, doi:10.2202/1544-6115.1175.
- Schumacher, S., and D. Breuer (2006a), Influence of a variable thermal conductivity on the thermochemical evolution of Mars, *J. Geophys. Res.*, **111**, E02006, doi:10.1029/2005JE002429.
- Schumacher, S., and D. Breuer (2006b), Correction to “Influence of a variable thermal conductivity on the thermochemical evolution of Mars,” *J. Geophys. Res.*, **111**, E09011, doi:10.1029/2006JE002755.
- Schumacher, S., and D. Breuer (2007), An alternative mechanism for recent volcanism on Mars, *Geophys. Res. Lett.*, **34**, L14202, doi:10.1029/2007GL030083.
- Simons, F. J., M. T. Zuber, and J. Korenaga (2000), Isostatic response of the Australian lithosphere: Estimation of effective elastic thickness and anisotropy using multitaper spectral analysis, *J. Geophys. Res.*, **105**, 19,163–19,184, doi:10.1029/2000JB900157.
- Simons, M., S. C. Solomon, and B. H. Hager (1997), Localization of gravity and topography: Constraints on the tectonics and mantle dynamics of Venus, *Geophys. J. Int.*, **131**, 24–31, doi:10.1111/j.1365-246X.1997.tb00593.x.
- Smith, D. E., et al. (2001), Mars Orbiter Laser Altimeter: Experiment summary after the first year of global mapping of Mars, *J. Geophys. Res.*, **106**, 23,689–23,722, doi:10.1029/2000JE001364.
- Smrekar, S. E., R. Comstock, and F. S. Anderson (2003), A gravity survey of Type 2 coronae on Venus, *J. Geophys. Res.*, **108**(E8), 5090, doi:10.1029/2002JE001935.

- Solomon, S. C., and J. W. Head (1990), Heterogeneities in the thickness of the elastic lithosphere of Mars: Constraints on heat flow and internal dynamics, *J. Geophys. Res.*, **95**, 11,073–11,083, doi:10.1029/JB095iB07p11073.
- Swain, C. J., and J. F. Kirby (2003), The coherence method using a thin anisotropic elastic plate model, *Geophys. Res. Lett.*, **30**(19), 2014, doi:10.1029/2003GL018350.
- Tarantola, A. (2005), *Inverse Problem Theory and Methods for Model Parameter Estimation*, SIAM, Philadelphia.
- Thomson, D. J., and A. D. Chave (1991), Jackknifed error estimates for spectra, coherences, and transfer functions, in *Advances in Spectral Analysis and Array Processing*, vol. 1, edited by S. Haykin, pp. 58–113, Prentice Hall, Englewood Cliffs, N. J.
- Turcotte, D. L., and G. Schubert (2002), *Geodynamics*, 2nd ed., Cambridge Univ. Press, Cambridge, U. K.
- Turcotte, D. L., R. J. Willemann, W. F. Haxby, and J. Norberry (1981), Role of membrane stresses in the support of planetary topography, *J. Geophys. Res.*, **86**, 3951–3959, doi:10.1029/JB086iB05p03951.
- Werner, S. C. (2009), The global Martian volcanic evolutionary history, *Icarus*, **201**, 44–68, doi:10.1016/j.icarus.2008.12.019.
- Werner, S. C., and K. L. Tanaka (2011), Redefinition of the crater-density and absolute-age boundaries for the chronostratigraphic system of Mars, *Icarus*, **215**, 603–607, doi:10.1016/j.icarus.2011.07.024.
- Wieczorek, M. (2007), Gravity and topography of the terrestrial planets, in *Treatise on Geophysics*, vol. 10, *Planets and Moons*, edited by T. Spohn, pp. 165–206, Cambridge Univ. Press, Cambridge, U. K., doi:10.1016/B978-0-444-52748-6.00156-5.
- Wieczorek, M. A. (2008), Constraints on the composition of the Martian south polar cap from gravity and topography, *Icarus*, **196**, 506–517, doi:10.1016/j.icarus.2007.10.026.
- Wieczorek, M. A., and R. J. Phillips (1998), Potential anomalies on a sphere: Applications to the thickness of the lunar crust, *J. Geophys. Res.*, **103**, 1715–1724, doi:10.1029/97JE03136.
- Wieczorek, M. A., and F. J. Simons (2005), Localized spectral analysis on the sphere, *Geophys. J. Int.*, **162**, 655–675, doi:10.1111/j.1365-246X.2005.02687.x.
- Wieczorek, M. A., and F. J. Simons (2007), Minimum-variance multitaper spectral estimation on the sphere, *J. Fourier Anal. Appl.*, **13**, 665–692, doi:10.1007/s00041-006-6904-1.
- Wieczorek, M. A., and M. T. Zuber (2004), Thickness of the Martian crust: Improved constraints from geoid-to-topography ratios, *J. Geophys. Res.*, **109**, E01009, doi:10.1029/2003JE002153.
- Willemann, R. J., and D. L. Turcotte (1982), The role of lithospheric stress in the support of the Tharsis rise, *J. Geophys. Res.*, **87**, 9793–9801, doi:10.1029/JB087iB12p09793.
- Williams, J.-P., D. A. Paige, and C. E. Manning (2003), Layering in the wall rock of Valles Marineris: intrusive and extrusive magmatism, *Geophys. Res. Lett.*, **30**(12), 1623, doi:10.1029/2003GL017662.
- Williams, J.-P., F. Nimmo, W. B. Moore, and D. A. Paige (2008), The formation of Tharsis on Mars: What the line-of-sight gravity is telling us, *J. Geophys. Res.*, **113**, E10011, doi:10.1029/2007JE003050.
- Wilson, L., and J. W. Head, III (1994), Mars: Review and analysis of volcanic eruption theory and relationships to observed landforms, *Rev. Geophys.*, **32**, 221–263, doi:10.1029/94RG01113.
- Witbeck, N. E., K. L. Tanaka, and D. H. Scott (1991), Geologic map of the Valles Marineris region, Mars, *U.S. Geol. Surv. Misc. Invest. Ser. Map*, **1-2010**.
- Zuber, M. T., and P. J. Mouginis-Mark (1992), Caldera subsidence and magma chamber depth of the Olympus Mons volcano, Mars, *J. Geophys. Res.*, **97**, 18,295–18,307, doi:10.1029/92JE01770.

M. Beuthe, V. Dehant, S. Le Maistre, and P. Rosenblatt, Royal Observatory of Belgium, Av. Circulaire 3, B-1180 Brussels, Belgium. (mikaël.beuthe@oma.be; veronique.dehant@oma.be; sebastien.lemaistre@oma.be; pascal.rosenblatt@oma.be)

M. Pätzold, Rheinisches Institut für Umweltforschung, Abteilung Planetenforschung, an der Universität zu Köln, Aachener Str. 209, D-50931 Köln, Germany. (martin.paetzold@uni-koeln.de)